remote sensing

MDPI

Article

Interacting Factors Controlling Total Suspended Matter Dynamics and Transport Mechanisms in a Major River-Estuary System

Zebin Tang [1], Yeping Yuan [1,*], Shuangyan He [1,2] and Yingtien Lin [1]

[1] State Key Laboratory of Ocean Sensing & Ocean College, Zhejiang University, Zhoushan 316021, China; thzebb@zuaa.zju.edu.cn (Z.T.); hesy@zju.edu.cn (S.H.); kevinlin@zju.edu.cn (Y.L.)
[2] Hainan Provincial Observatory of Ecological Environment and Fishery Resource in Yazhou Bay, Sanya 572025, China
* Correspondence: yyping@zju.edu.cn

Highlights

What are the main findings?

- Developed an improved Total Suspended Matter (TSM) retrieval algorithm using an expanded dataset, significantly enhancing accuracy and generalizability for highly turbid coastal waters.
- Elucidating the synergistic interactions of tides, monsoon winds, and ocean currents (Jiangsu Alongshore Current, Taiwan Warm Current, and Yellow Sea Warm Current) that control TSM dynamics, this work uncovered a previously unresolved offshore TSM transport pathway, challenging the conventional nearshore transport paradigm.

What is the implication of the main finding?

- The accurate satellite retrieval algorithm enables reliable and continuous monitoring of sediment dynamics in a river–estuary system.
- The insights into the interactions of key factors and the pathways of TSM plumes offer a robust scientific foundation for enhancing environmental monitoring strategies and optimizing coastal management practices.

Abstract

The Changjiang estuary–Hangzhou Bay region is a critical zone of land–sea interaction, where Total Suspended Matter (TSM) dynamics significantly influence coastal ecology and engineering. While previous studies have examined individual factors affecting TSM variability, the synergistic effects of "tide–monsoon–current" interactions and the actual pathways of turbid plume transport remain poorly understood. Using GOCI satellite data, in situ buoy measurements, and voyage data from 2020, this study applied Data Interpolating Empirical Orthogonal Functions (DINEOFs) and comprehensive spatio-temporal analysis to reconstruct continuous high-resolution TSM fields and elucidate multi-factor controls on TSM dynamics. Based on this high-resolution dataset of TSM, we found that, during the dry season, elevated TSM concentrations are primarily driven by wind–tide resuspension and transport under the comprehensive forcing of the Jiangsu Alongshore Current (JAC), the Yellow Sea Warm Current (YSWC), and wind–tide-induced flows. Contrary to the conventional understanding, the Jiangsu-origin surface TSM can transport to the outer sea without supplementing the TSM in the Turbidity Maximum Zone (TMZ). The YSWC in autumn can cause either low C_{TSM} gradients or high gradients nearshore depending on whether it is carrying Korean coastal turbid water or not. During the wet

Check for updates

Academic Editor: Dong Liu

Received: 10 September 2025
Revised: 14 December 2025
Accepted: 24 December 2025
Published: 5 January 2026

Copyright: © 2026 by the authors. Licensee MDPI, Basel, Switzerland. This article is an open access article distributed under the terms and conditions of the Creative Commons Attribution (CC BY) license.

season, stratification induced by the Changjiang freshwater discharge suppresses wind–tide resuspension, reducing TSM concentrations in the TMZ and the Qidong water. However, the Changjiang freshwater combined with the Taiwan Warm Current (TWC) dilutes surface TSM in Hangzhou Bay, where the two water masses meet on the 10 m isobath. These insights into factor interactions and TSM plume pathways provide a scientific basis for improved environmental monitoring and coastal management.

Keywords: Changjiang estuary; Hangzhou Bay; total suspended matter; remote sensing; controlling mechanisms

1. Introduction

A Total Suspended Matter (TSM) of high concentration is the distinct feature of coastal waters and, on the one hand, has a significant impact on underwater lighting, which controls biological productivity [1–4]. On the other, TSM releases nitrogen elements into the coastal waters, which becomes nutritional dissolved inorganic nitrogen or materials for heterotrophic reactions [5–7]. Moreover, TSM dynamics profoundly influence the erosion and siltation of port waterways and the evolution of the terrain [8,9]. Hangzhou Bay, China, connects northward to the turbid topographically complex Changjiang (or the old name "Yangtze" in other literature) estuary. The region of Hangzhou Bay to the Changjiang estuary (Figure 1) is a vital part of China's "Changjiang River Delta" economic belt, exhibiting exceptionally high TSM concentrations in the waters. The surface TSM concentration at the top of Hangzhou Bay during spring tides can reach 10.6 kg/m^3 [10] and the Changjiang estuary shapes the transport path of heavy metal elements as well as the timing and the location of algal outbreaks [11,12]. Therefore, the study of TSM dynamics in the region will provide important references for economic activities and environmental protection there.

Among the methods of studying the TSM dynamics, traditional field sampling can hardly synoptically map the wide spatial and temporal variability of TSM. Hence, satellite ocean color data have been being utilized to map TSM dynamics in the coastal waters over recent years [13–16]. However, limitations in the accuracy and consistency of TSM retrieval algorithms hinder the precise characterization of surface TSM dynamics across the estuary–bay continuum. TSM data are included in the GOCI data products, whereas its built-in algorithms of TSM inversion lose efficacy when faced with Chinese coastal waters with high turbidity, causing an urgent need for a new TSM inversion algorithm to study the high turbidity waters. In addition, the TSM inversion data are so affected by cloud covering that the available inversion dataset was severely limited in the previous studies [13–18], which led to a low temporal continuity due to the data gaps.

On different time scales, the TSM in the study area is subject to variable controlling processes. Within a tidal cycle, the tide is one of the main factors controlling the diurnal dynamics of the TSM [14–16,19]. In the water of the Zhoushan Archipelago, part of the Hangzhou Bay, TSM concentration generally varies within 2 h after tidal level change [16], and the time lag is mainly due to tidal mixing intensity and water depth [20,21]. The Changjiang estuary becomes a source or sink of TSM periodically, due to the transformation of spring and neap tides [19]. On the seasonal scale, firstly, the transport direction of the TSM plume from the Changjiang estuary is consistent with the wind directions in the corresponding seasons [22]. Windborne waves enhance the resuspension and vertical mixing of water columns in the Changjiang estuary and Hangzhou Bay, resulting in a higher concentration of TSM than in summer [23,24]. Secondly, from Xuliujing to the

South Branch in the Changjiang estuary, the TSM concentration is generally higher in the summer than in the winter, while, due to the dilution and stratification of Changjiang runoff, the concentration of TSM in the south of the estuary is lower in the summer than in the winter [23,25–27]. Furthermore, driven by the Jiangsu Alongshore Current (JAC), the turbid water along the Qidong coast can reach the near shore of the Changjiang estuary in the winter; in the summer, however, the clear water of the Taiwan Warm Current (TWC) causes the water to be of high TSM concentration along the Qidong shore to retreat to the northwest [23,28]. The paths of the JAC and TWC are shown in Figure 1b.

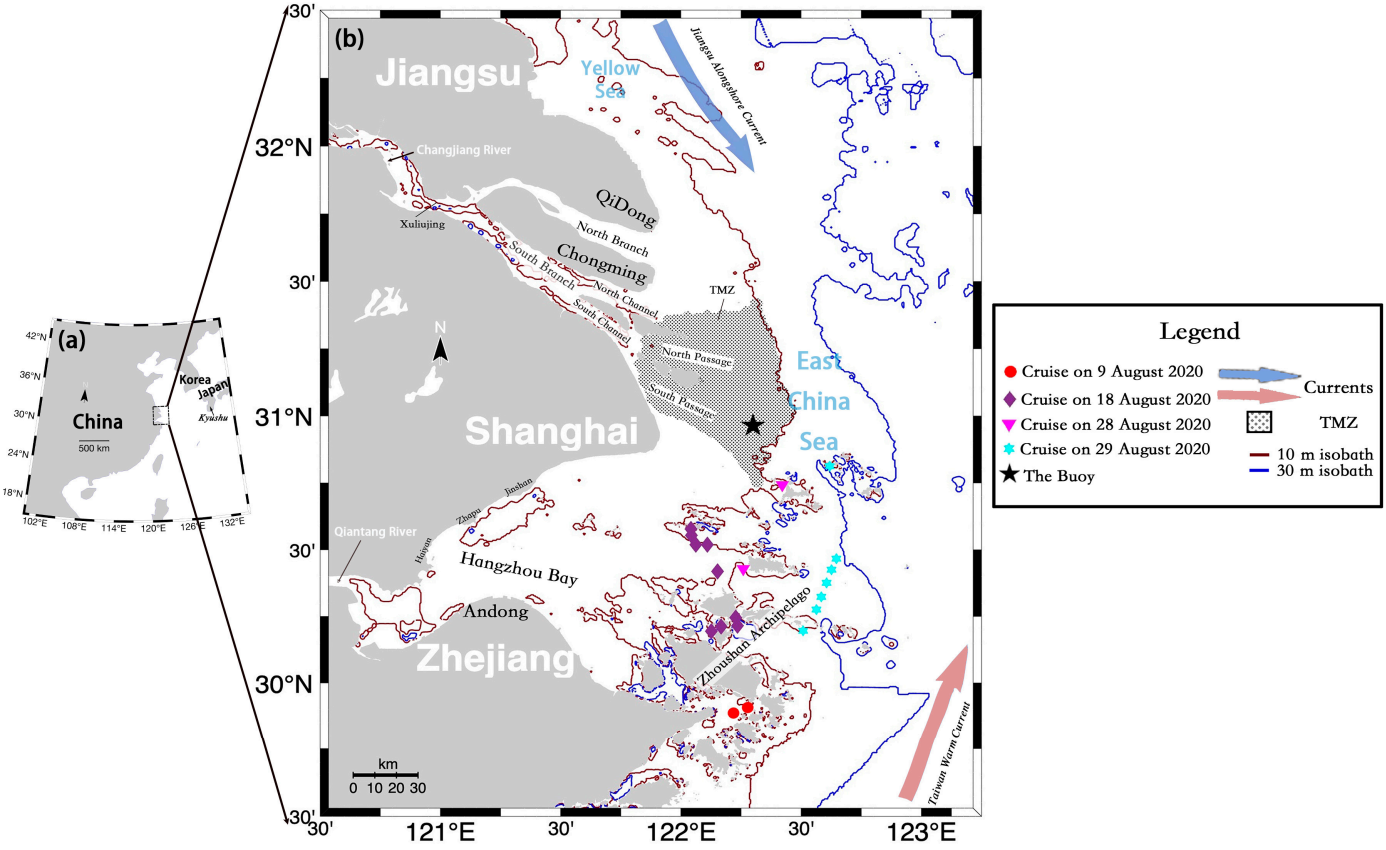

Figure 1. The location (**a**) and the map of the study region (**b**). The dotted part in (**b**) is for the Turbidity Maximum Zone (TMZ), and the two large arrows represent the Jiangsu Alongshore Current (JAC) and the Taiwan Warm Current (TWC). The pentagram and other geometrical icons denote the buoy and the voyages collecting in situ TSM data, respectively, on different dates, 2020.

However, many of these studies above discussed the influence of the environmental factors in a limited number [14–16,19–22]. The great difference in temporal and spatial variation in TSM in the Changjiang estuary and Hangzhou Bay indicates that a single environmental factor cannot resolve the dynamics of surface TSM. Shen et al. [23] made a relatively comprehensive analysis of the environmental factors affecting the surface TSM in the study area, but more details are still in need of further clarification: the TSM plume paths between the Changjiang estuary and the Jiangsu coast can be dug deeper; the interactions between the Changjiang runoff and the TWC in wet season are still not sufficiently clarified; and, besides the JAC and TWC, the potential patterns of other background ocean currents need elaborating further. At the same time, the accuracy algorithms of TSM inversion at present are various, but there is still a large room for improvement, which also leads to the lack of resolution of the spatial and temporal dynamics of surface TSM in the Changjiang estuary–Hangzhou Bay.

Based on the voyage, buoy, and GOCI data in the year of 2020, this study attempts to build a dataset with high resolution and accuracy and without the data gaps caused by cloud covering. The study addresses these gaps by comprehensively analyzing the multi-factor controls on surface TSM spatio-temporal patterns in the Changjiang estuary–Hangzhou Bay region. The remainder of this paper is structured as follows: Section 2 details the data sources. Section 3 describes the atmospheric correction and cloud-impact mitigation via interpolation. Section 4 presents the validation of TSM retrieval and the Data Interpolating Empirical Orthogonal Functions (DINEOFs), and subsequently presents the observed TSM distribution patterns. Section 5 discusses the underlying mechanisms. Conclusions are summarized in Section 6.

2. Study Area and Data Sources

2.1. Study Area

The study area is within the range of about 120.5°~123°E, 29.5°~32.5°N (Figure 1b). The Changjiang estuary, the northern water of the area, comprises Xuliujing, the North and South Branch, the North and South Channel, the North and South Passage, and the Turbidity Maximum Zone (TMZ), from the northwest to the southeast. The TMZ is characterized by higher TSM concentration (simplified as "C_{TSM}", mg/L) than that in the encircling estuarine parts, the formation of which is mainly related to the resuspension of small particles of TSM [29–31]. The water to the north of the Qidong cape is the Yellow Sea, where there is seasonal horizontal substance exchange between the Jiangsu coast and the Changjiang estuary [23].

The East China Sea is to the south of the Qidong Cape and Hangzhou Bay is located farther south. Wu et al. [32] reported that 40% of the matter from the Changjiang estuary is deposited in Hangzhou Bay and the adjacent waters; however, only a very small portion of the matter discharged from the Qiantang River is transported into Hangzhou Bay [27,33]. The top of Hangzhou Bay contracts rapidly, characterized by a persistent high concentration of TSM [9,15].

2.2. In Situ Data

The in situ dataset consists of buoy (multi-parameter water quality sensor YSI EXO2) measurements and voyage-collected samples. Buoy data (located in the pentagram in Figure 1b), provided by He et al. [18], span 1 January to 31 December 2020 (00:00–23:00), with turbidity recorded in Nephelometric Turbidity Units (NTUs). Previous studies [34–36] have established a robust linear relationship between NTUs and C_{TSM}. Among them, Tang et al. [35] used buoy data from the Changjiang estuary and Hangzhou Bay to validate satellite-derived C_{TSM} (GOCI and TG-2/WIS) following the relationships between NTUs and C_{TSM} proposed by Zhao et al. [34], which indicate that the buoy data are applicable for validating GOCI data in the Changjiang estuary and Hangzhou Bay where the C_{TSM} can be 2000 mg/L or more. Hence, NTU values in this study were converted to C_{TSM} (mg/L) using the seasonally differentiated relationships [34]: $C_{TSM} = 2.1 \times NTU^{\circ}$ (dry season) and $C_{TSM} = 1.3 \times NTU^{\circ}$ (flood season). After being converted to C_{TSM}, the minimum was 4 mg/L, the maximum 1665 mg/L, and the mean value was 178 mg/L.

Voyage data were sourced from Du et al. [16], collected during August 2020 along routes shown in Figure 1b. The voyage data covered the processes of spring tide, neap tide, high tide, and low tide, and also included the periods of the spring–neap tidal cycle. The subsequent laboratory processing involved the following: (1) drying clean glass fiber filters at 40 °C for 8 h; (2) cooling and weighing filters to 0.0001 g precision; (3) filtering 500 mL samples under vacuum; (4) rinsing filters three times with distilled water to remove

dissolved salts; (5) redrying filters at 40 °C for 24 h; and (6) reweighing cooled filters to determine in situ C_{TSM}.

The details of the in situ data are listed in Table 1 below.

Table 1. Location and time of the in situ sampling in Figure 1b.

Buoy/Voyage	Location	Time
The Buoy (YSI EXO2)	122.29980°E, 30.96472°N	00:00~23:00 (hourly, 1 January to 31 December 2020)
Voyage Sampling 1	122.277397°E, 29.907597°N	12:42 9 August 2020
Voyage Sampling 2	122.219218°E, 29.887366°N	13:00 9 August 2020
Voyage Sampling 3	122.126600°E, 30.195296°N	08:20 18 August 2020
Voyage Sampling 4	122.166927°E, 30.211592°N	08:30 18 August 2020
Voyage Sampling 5	122.235503°E, 30.215261°N	08:50 18 August 2020
Voyage Sampling 6	122.227423°E, 30.245228°N	09:05 18 August 2020
Voyage Sampling 7	122.151808°E, 30.419482°N	10:09 18 August 2020
Voyage Sampling 8	122.062192°E, 30.518795°N	10:39 18 August 2020
Voyage Sampling 9	122.044493°E, 30.554126°N	10:49 18 August 2020
Voyage Sampling 10	122.041208°E, 30.578692°N	15:18 18 August 2020
Voyage Sampling 11	122.110332°E, 30.518420°N	15:39 18 August 2020
Voyage Sampling 12	122.258925°E, 30.428798°N	11:53 28 August 2020
Voyage Sampling 13	122.420865°E, 30.743372°N	13:48 28 August 2020
Voyage Sampling 14	122.618398°E, 30.813056°N	08:34 29 August 2020
Voyage Sampling 15	122.645817°E, 30.466449°N	13:41 29 August 2020
Voyage Sampling 16	122.626067°E, 30.425859°N	13:51 29 August 2020
Voyage Sampling 17	122.605377°E, 30.376142°N	14:03 29 August 2020
Voyage Sampling 18	122.583357°E, 30.323540°N	14:16 29 August 2020
Voyage Sampling 19	122.563234°E, 30.276683°N	14:28 29 August 2020
Voyage Sampling 20	122.508965°E, 30.196032°N	14:50 29 August 2020

2.3. Remote Sensing Data

Remote sensing data comprised Level 1B (L1B) products in HDF5 format, acquired from the Geostationary Ocean Color Imager (GOCI) and downloaded via the Korea Ocean Satellite Center (KOSC) website (kosc.kiost.ac.kr). Launched in 2010, GOCI occupies a geostationary orbit, providing high-frequency observations of a 2500 km × 2500 km area (116.08°~143.92°E, 24.75°~47.25°N) encompassing much of East Asia. This extensive spatial coverage and stationary vantage point make GOCI particularly valuable for monitoring regional seas. The sensor features eight spectral bands centered at 412, 443, 490, 555, 660, 680, 745, and 865 nm. It acquires eight images daily at hourly intervals from 08:28 to 15:28 (GMT+8), each with a 500 m spatial resolution. For this study, L1B data were processed to Level 2 (L2) using the GOCI Data Processing System (GDPS), yielding derived products including Rayleigh-corrected reflectance and satellite zenith angles.

2.4. Other Data

Surface TSM dynamics is under the control of environmental factors, whose detailed data introduction is shown below in Table 2.

Table 2. Environmental factor data details.

Data	Source	Details
Hourly Wind Stress	https://data.marine.copernicus.eu/product/WIND_GLO_PHY_L4_MY_012_006/download (accessed on 14 April 2025)	The instantaneous components of sea surface wind stress (N/m^2) in 2020, calculated from the wind speed 10 m over the sea surface, with a time resolution of 1 h and a spatial resolution of 0.125 latitude and longitude. The data were linearly interpolated to obtain a higher spatial resolution in this study by means of the Delaunay triangulation of scattered sample points.
Daily Changjiang River Runoff	By courtesy of Bureau of Hydrology, Changjiang Water Resources Commission, Ministry of Water Resources	The daily average runoff of Datong Station on the Changjiang River from 1 January 2020 to 31 December 2020.
Current	https://data.marine.copernicus.eu/product/MULTIOBS_GLO_PHY_MYNRT_015_003/download?dataset=cmems_obs-mob_glo_phy-cur_my_0.25deg_PT1H-i_202411 (accessed on 14 April 2025)	Hourly data for tide current and resultant current (geostrophic velocity + Ekman driven velocity + tide velocity) span 1 January to 31 December 2020 (00:00–23:00) with the spatial resolution of 0.25 degrees of longitude and latitude. The data were linearly interpolated to obtain a higher spatial resolution in this study by means of the Delaunay triangulation of scattered sample points.
Salinity	https://data.marine.copernicus.eu/product/GLOBAL_MULTIYEAR_PHY_001_030/download (accessed on 1 December 2025)	Surface sea salinity, from 1 January to 31 December 2020, with unit of psu. The data were linearly interpolated to obtain a higher spatial resolution in this study by means of the Delaunay triangulation of scattered sample points.

3. Methods

The methods used in this paper to process the raw data and obtain the analyzable remote sensing data can be mainly divided into two aspects: (1) data collection and preprocessing and (2) data postprocessing.

For data collection and preprocessing, the remote sensing reflectance was obtained from the raw data by means of atmospheric correction (details can be found in Section 3.1). It is inevitable that remote sensing data are impacted by cloud coverage, which leads to missing data and noise. For data postprocessing, therefore, the TSM retrieved was interpolated and smoothed to make up the missing data and eliminate the noise that overestimates the results (details can be found in Section 3.2).

3.1. Atmospheric Correction

Previous works have proved that there exists a linear relationship between the ratio of GOCI Band 7 to Band 3 (B7/B3) and the C_{TSM} at logarithmic scale in the Changjiang estuary–Hangzhou Bay area [13,14,16,37].

Based on the algorithm of He et al. [13] and He et al. [14], the *Ratio* (B7/B3) was calculated as the following:

$$Ratio = \frac{R_{rs}(745\ \text{nm})}{R_{rs}(490\ \text{nm})} \quad (1)$$

In Equation (1), R_{rs} is the remote sensing reflectance, and 745 nm and 490 nm are the wavelengths λ of Band 7 and Band 3, respectively. Through Equation (2), R_{rs} is calculated as follows:

$$R_{rs}(\lambda) = \frac{\rho_w(\lambda)}{t_s(\lambda) \times \pi} \quad (2)$$

where ρ_w is the water-leaving reflectance and t_s is the diffuse transmission coefficient from the sun to the sea surface. ρ_w is calculated through Equation (3):

$$\rho_w(\lambda) = \frac{\rho_{rc}(\lambda) - \rho_{rc}(865\ \text{nm})}{t_v(\lambda)} \quad (3)$$

ρ_{rc} is the Rayleigh-corrected reflectance, which can be obtained by loading GOCI L2C files. t_s in (2) and t_v, the diffuse transmission coefficient from the sea surface to the satellite sensor, in (3) can be calculated using the Rayleigh optical thickness and ozone concentration through Equation (4), based on the fact that the observation zenith angle of GOCI is less than 60° in the study area and the aerosol transmittance can be ignored and taken to the value of 1 [38]:

$$t(\theta, \lambda) = exp[-(\frac{\tau_r(\lambda)}{2} + \tau_{oz}(\lambda))(\frac{1}{cos\theta})] \quad (4)$$

Here, θ is the solar zenith angles or the satellite zenith angles for estimating t_s and t_v, respectively. τ_r is the Rayleigh optical thickness, and τ_{oz} is the ozone optical thickness, both of which can be found in the studies of Gordon et al. [38] and Tanaka et al. [39]. All the parameters in Equations (1)–(4) are summarized in Table 3 below for easy reference.

Table 3. Description of the parameters in Equations (1)–(4).

Parameter	Description
Ratio	Ratio of GOCI Band 7 to Band 3 used to calculate C_{TSM}
R_{rs}	Remote sensing reflectance used to calculate *Ratio*
λ	Light wavelength
ρ_w	Water-leaving reflectance
ρ_{rc}	Rayleigh-corrected reflectance
t_s	Diffuse transmission coefficient from the sun to the sea surface
t_v	Diffuse transmission coefficient from the sea surface to the satellite sensor
θ	Solar zenith angles or the satellite zenith used to obtain t_s and t_v
τ_r	Rayleigh optical thickness
τ_{oz}	Ozone optical thickness

3.2. Gaps Filling and Smoothing of Remote Sensing Derived C_{TSM}

Cloud covering and other obstructions inevitably lead to spatial gaps in the TSM distribution maps derived from GOCI data. These data gaps hinder the comprehensive analysis of spatio-temporal TSM dynamics and their controlling mechanisms. To reconstruct these missing values, the DINEOF method was employed.

DINEOF is a robust gap-filling technique specifically designed for spatio-temporal datasets common in oceanography and remote sensing. It reconstructs missing data by iteratively decomposing the data field using Singular Value Decomposition (SVD). The algorithm progressively incorporates additional Empirical Orthogonal Functions (EOFs) into the reconstruction of gappy regions, optimizing the solution by minimizing the reconstruction error when compared to a subset of known reference values (non-gap pixels),

where the reference values include different temporal data in the same location. This iterative process continues until convergence is achieved, typically defined by a minimal reduction in the root mean square error (RMSE) between iterations.

While DINEOFs successfully reconstruct the dominant spatio-temporal patterns of TSM, the resulting fields can retain noise inherent in the original GOCI imagery, manifesting as localized outliers. To mitigate these anomalous values, we applied a statistical filtering procedure. The interpolated TSM data were evaluated on a $0.1^\circ \times 0.1^\circ$ grid. Within each grid cell, values exceeding two standard deviations (2σ) above the cell's mean TSM concentration were identified as outliers. These outliers were subsequently replaced by the mean TSM value calculated for that specific $0.1^\circ \times 0.1^\circ$ grid cell, effectively smoothing the data while preserving the underlying spatial structure reconstructed by DINEOFs.

4. Results

4.1. TSM Calculation and Validation

In this section, the in situ data, including a long-term in situ observational TSM time series (the buoy data) and large area in situ observational TSM data (the voyage data), are utilized to validate and to calibrate the previous retrieval algorithms, aimed at obtaining more precise spatio-temporal distributions of TSM and furthermore analyzing the complex controlling mechanisms of TSM dynamics.

Using Equations (1)–(4), *Ratio* was estimated, then C_{TSM} could be calculated through Equation (5):

$$C_{TSM} = 10^{a \times Ratio + b} \quad (5)$$

where a and b were the constants to be trained. After data cleansing, when the *Ratio*s accordingly with the buoy data and the voyage data were removed due to the cloud noise causing over-estimation of the *Ratio*, we obtained 20 voyage data and 761 buoy data, whose spatial distribution is shown in Figure 1b. Then, the data were randomly split into the training data set and the validation dataset at the ratio of 1:1. To match the in situ data to the GOCI remote sensing reflectance data, the time window was set to within 1 h and the remote sensing reflectance was the spatially mean values within the circle areas of about 0.3 km^2 whose centers with the radius of 0.003 longitude and latitude were located at the positions of the in situ data. The in situ TSM distribution are shown in Figure 2 below.

The maximum, the minimum, and the median of the in situ TSM are 1203, 12, and 56 mg/L, respectively. It can be seen from Figure 2 that the majority of the concentrations are below 250 mg/L but that the ultra-high concentrations are over 1000 mg/L, which magnifies the difficulty of precisely mapping the TSM dynamics in the Changjiang estuary–Hangzhou Bay region.

Based on Equation (5), Equation (6) was derived as below:

$$log_{10}(C_{TSM}) = a \times Ratio + b \quad (6)$$

Formula (6) reveals that *Ratio* keeps a linear relation with the logarithm of the in situ TSM, as shown in Figure 3.

The p-value in Figure 3 is less than 0.05 with R^2 at 0.86 and RMSE at 0.19, indicating a remarkable linear relation consistent with the previous studies [13,14,16,37].

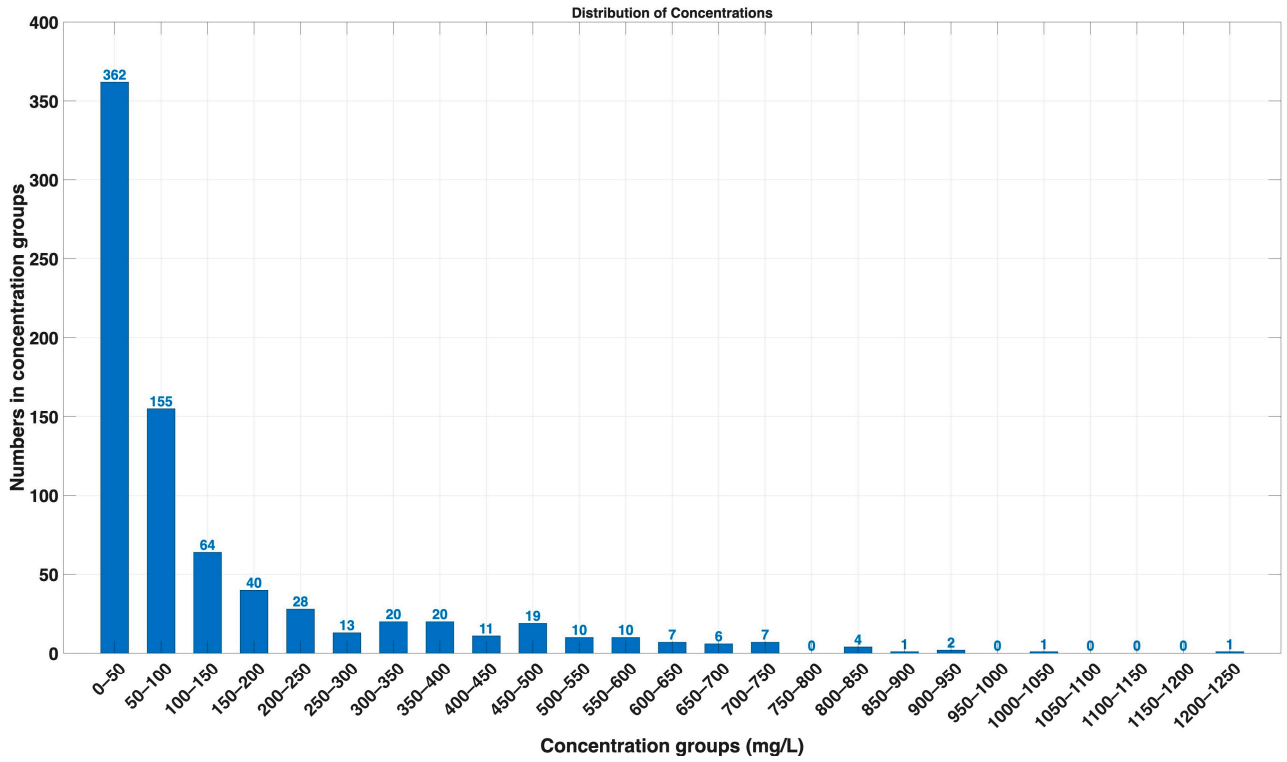

Figure 2. The distribution of in situ TSM concentrations. The interval of the concentration groups is left-closed and right-open.

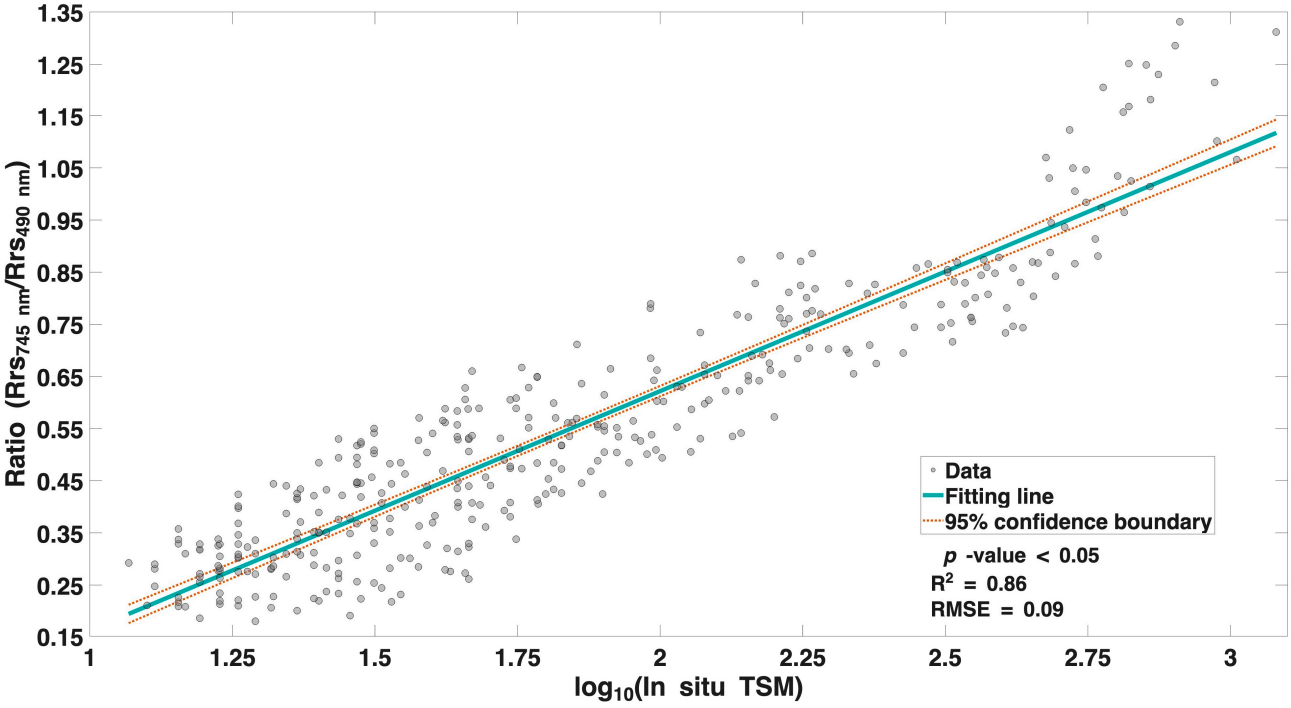

Figure 3. The relation between the remote sensing reflectance ratio and the algorithm training data.

By means of Ordinary Least Squares based on the training dataset, a and b were subsequently estimated 1.8689 and 0.8151. The validation of the retrieval algorithms was then conducted, as shown in Figure 4. The algorithm of He et al. [14] underestimated the C_{TSM} overall, whereas the algorithm of Du et al. [16] overestimated the C_{TSM} when the C_{TSM} was under about 100 mg/L and underestimated it when the C_{TSM} was over

100 mg/L. The retrieval algorithm in this paper, however, retained high precision from the low C_{TSM} to the high C_{TSM}.

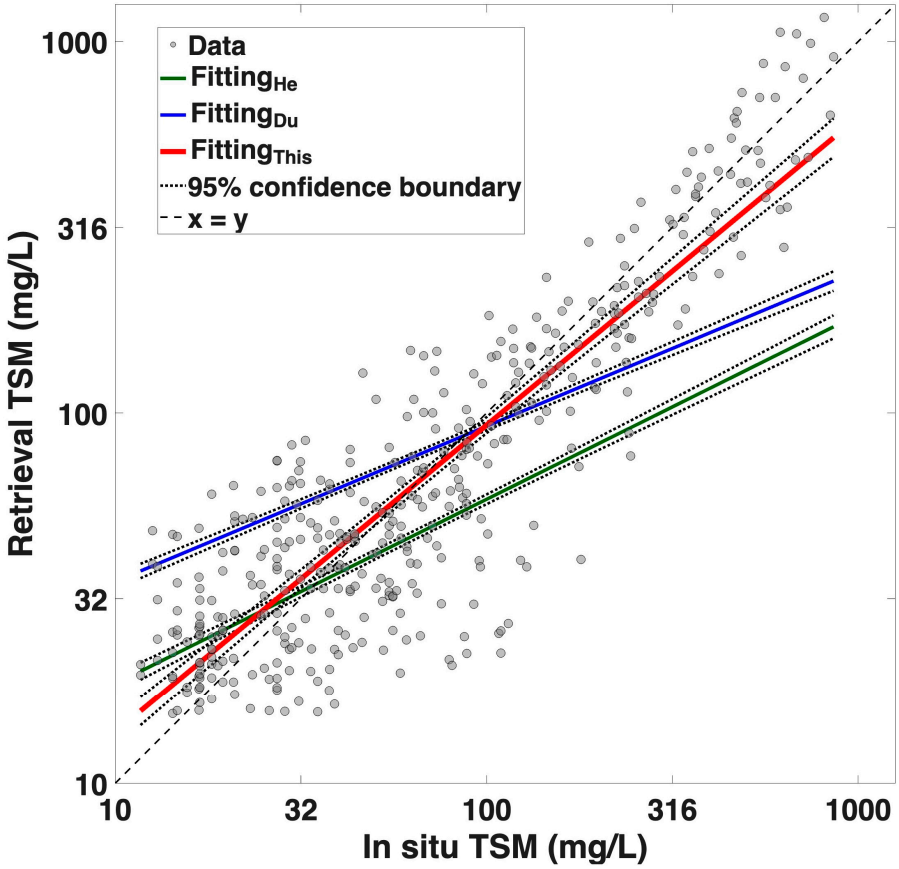

Figure 4. Validation of the retrieval algorithms. The subscripts "He", "Du", and "This" denote the results obtained from the algorithms of He et al. [14], Du et al. [16], and this study, respectively. The scales on the axes are even at the logarithms to the base of 10.

Compared to the dataset size for algorithm training and the degree of freedom for algorithm validation of 343, 41 and 61, 74 of He et al. [14] and Du et al. [16], respectively, there was a much higher degree of freedom of validation and a larger training dataset in this paper (Table 4), which suggests a stronger robustness in the algorithm.

Table 4. The comparison of the retrieval algorithms in He et al. [14], Du et al. [16], and this study. The three studies apply the same retrieval algorithm as Formula (5) depicts but with different *a* and *b*.

Algorithm	*a*, *b*	R^2	*p*-Value	RMSE (mg/L)	Dataset Size for Algorithm Training	Degree of Freedom for Algorithm Validation in Their Original Studies
He et al. [14]	1.1230, 1.0758	0.60	<0.05	140	343	41
Du et al. [16]	0.9456, 1.3820	0.61	<0.05	119	61	74
This Study	1.8689, 0.8151	0.78	<0.05	72	371	408

The C_{TSM} significantly differs during seasons with the different hydrodynamic conditions (flood or dry). The mean absolute percentage errors (MAPEs) of the retrieval C_{TSM} compared to the validation in situ data in this study are 20.89% in the flood season (June to August) and 19.49% in the dry season (other months). Furthermore, the MAPEs in different concentration ranges of the validation in situ data are listed in Table 5 below. Note that,

since the in situ data in Figure 2 are mainly distributed under 200 mg/L, the C_{TSM} ranges in the table are not even.

Table 5. Retrieval MAPE. The concentration intervals are left-closed and right-open.

In Situ C_{TSM} Range (mg/L)	[0, 50)	[50, 100)	[100, 150)	[150, 200)	[200, 550)	[550, 900)
MAPE	19.31%	20.82%	17.95%	19.36%	19.44%	25.26%

The MAPE in Table 5 exhibits minor variation, except that of the concentration between 550 and 900 mg/L, potentially caused by signal saturation [18], which indicates that the retrieval algorithm adopted in this paper is suitable for the study. The large training dataset and the large validating dataset used in the study covered both large temporal and spatial ranges, which suggests high generalization and precision of the retrieval algorithm and can reveal much truer TSM distribution and dynamics.

4.2. DINEOF Validation

We divided the dataset into training set and testing set with 80%: 20%, and three statistical metrics—correlation coefficient (R^2), root mean square error (RMSE), mean absolute difference (MAD)—were selected to test the performance of the DINEOF algorithm. For the testing set, the R^2 is 0.85, the RMSE is 157 mg/L, and the MAD is 124 mg/L. Thus, the DINEOF can be used to reconstruct the missing data in our study. Figure 5 shows the result of the reconstruction of the TSM gap values.

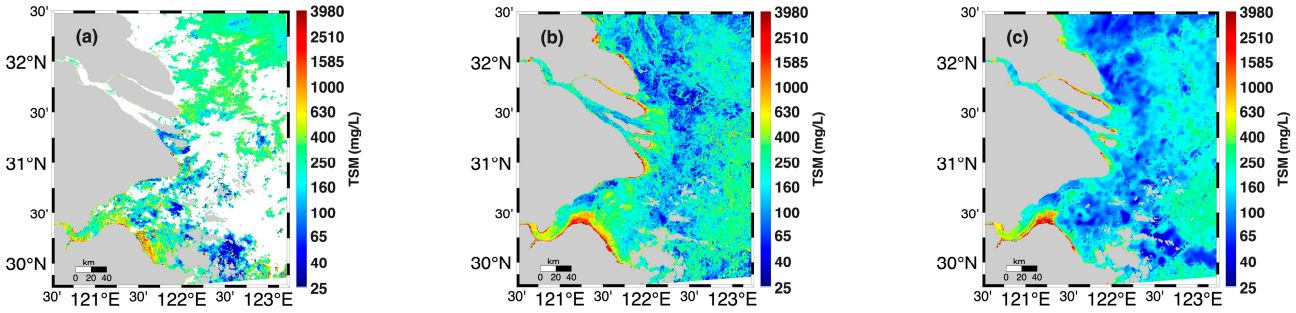

Figure 5. TSM maps of raw data (**a**), unsmoothed interpolated data (**b**), and smoothed interpolated data (**c**) on 9 July 2020.

Upon the reconstruction of the gaps in Figure 5a, the interpolated TSM was obtained. However, the distribution with much noise (Figure 5b) can hinder the interpretation of the actual TSM dynamics. Using the statistical filtering procedure mentioned in Section 3.2, we filtered the noise and obtained the smoothed distribution, as shown in Figure 5c.

4.3. Spatio-Temporal Distribution of TSM

Seasonally, domain-averaged C_{TSM} reached 436 mg/L in the spring, 246 mg/L in the summer (the annual minimum; Figure 6b), 489 mg/L in the autumn, and 574 mg/L in the winter. High-concentration waters (>250 mg/L) nearly covered Hangzhou Bay during the autumn and the winter (Figure 6c,d), while a clear-water band separating the 10 m isobath from the offshore TSM front displayed marked seasonal variability: maximally expansive during the spring and the summer, then contracting abruptly in the autumn as the TSM front advanced eastward, ultimately disappearing in the winter when the front achieved its furthest eastern extent.

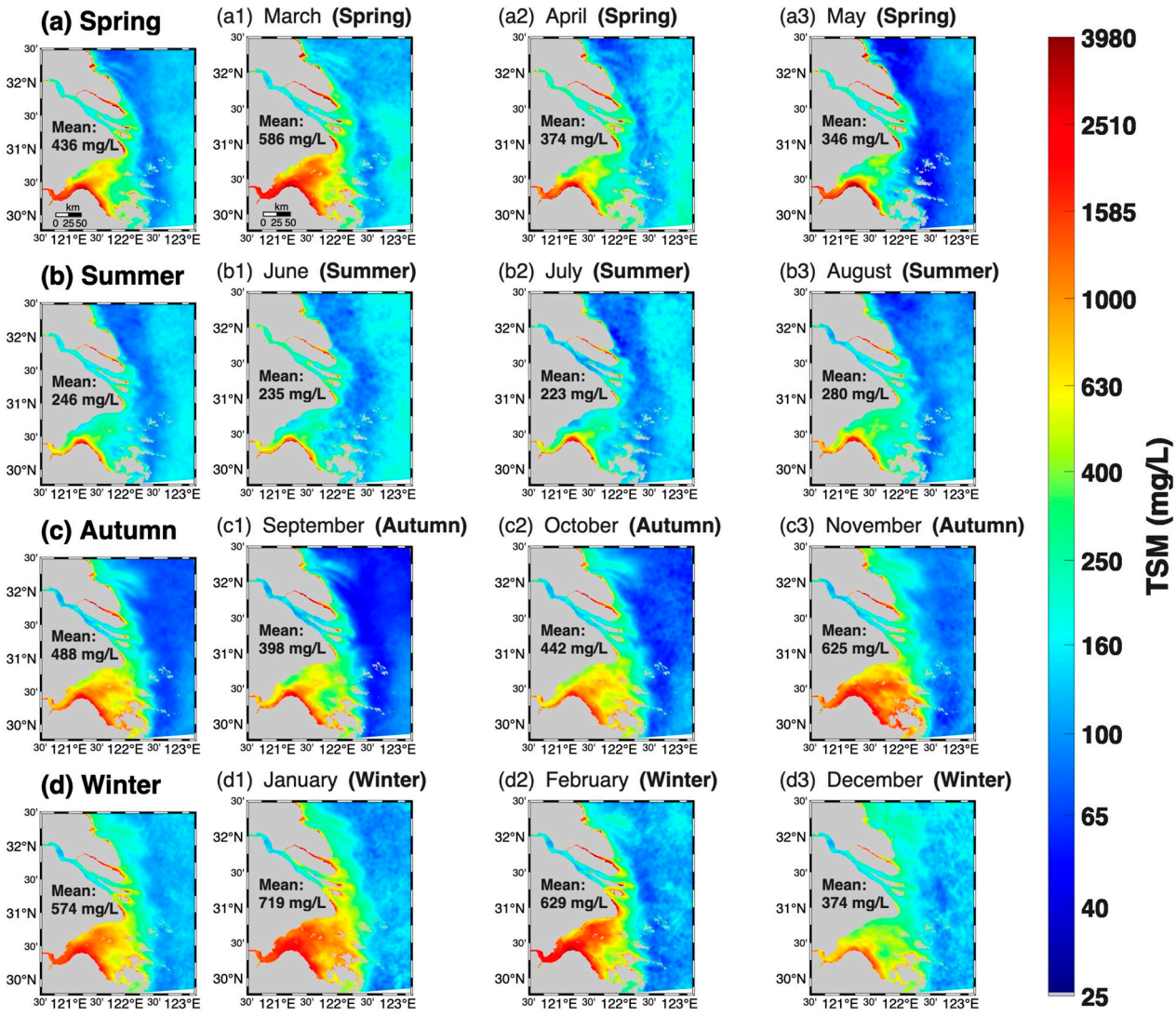

Figure 6. Seasonal and monthly spatial distributions of TSM in 2020. (**a**–**d**) represent the seasonal mean TSM maps from spring to winter and the figures with the numeric marks represent the monthly mean TSM maps for the three months in the according seasons (e.g., (**a1**–**a3**) for March to May in spring, (**b1**–**b3**) for June to August in summer, and so on). The scales are denoted in (**a**,**a1**), where the scale in (**a**) is for the seasonal mean TSM maps (i.e., for (**a**–**d**)) and the scale in (**a1**) for the monthly mean TSM maps (i.e., for (**a1**–**d3**)). The spatially mean C_{TSM} for the nearshore part of the study region (within the 10 m isobath north to 31°N and Hangzhou Bay with Zhoushan Archipelago included) is denoted.

Monthly resolution revealed additional dynamics. To demonstrate more details of the TSM dynamics, the nearshore part of the study region was divided into four blocks, as in Figure 7a. Temporally, the domain-averaged C_{TSM} for all the four blocks peaked in January (719 mg/L) and troughed in July (223 mg/L; the green curve in Figure 7b). Following a pronounced 212 mg/L decline between March and April, concentrations stabilized before rising steadily after July to a secondary November peak. A sharp December decrease of 251 mg/L—predominantly driven by reductions in Hangzhou Bay (Figure 6(c3,d3), the purple curve in Figure 7b)—returned system-wide C_{TSM} to April levels (374 mg/L). Generally, the temporal dynamics in most of the consisting blocks keep consistent with that of the nearshore region to some extent; however, the Xuliujing–South Branch shows some particularity. The C_{TSM} in the Xuliujing–South Branch met the summit at 256 mg/L (the orange curve in Figure 7b) in June and slumped to the lowest point one month later at

140 mg/L. It is reported that the C_{TSM} of the Xuliujing–South Branch usually reaches the top in summer according to its multi-year average [23].

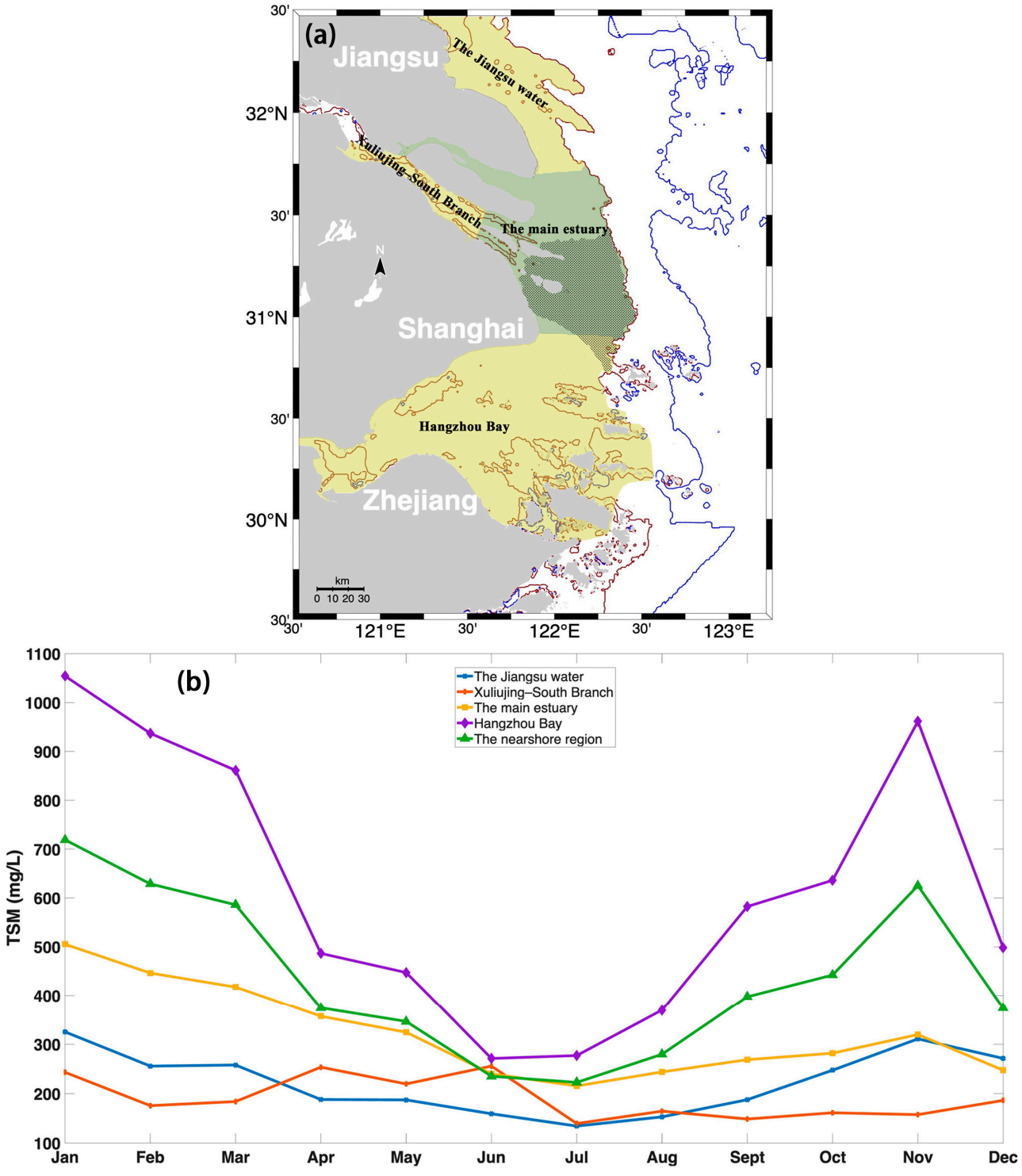

Figure 7. (**a**), the nearshore part of the study region consisting of the blocks "the Jiangsu water" (yellow), "Xuliujing–South Branch" (yellow), "the main estuary" (green), and "Hangzhou Bay" (yellow), where the colors (yellow/green) denote the areas the blocks cover and the dark red and the blue lines are the 10 m isobaths and the 30 m isobaths respectively as those in Figure 1; (**b**) monthly spatially mean C_{TSM} curves of the nearshore part of the study region and the consisting blocks, respectively.

Spatially, the clear-water band initiated westward incursion into previously turbid estuary zones in February (Figure 6(d1,d2)). This expansion continued through July alongside declining C_{TSM}, ultimately reaching the deeper Zhoushan Archipelago region (10–30 m isobaths). From August, turbid waters progressively reclaimed territory, contracting the clear-water band until completely occupying the 10 m isobath zone by November. Although December witnessed substantial C_{TSM} reduction, turbid waters maintained spatial dominance. The North Branch of the Changjiang estuary, along with the southern shoreline and apex of Hangzhou Bay, maintained persistently elevated surface TSM concentrations year-round. Notably, Hangzhou Bay exhibited the most pronounced monthly variability in TSM spatial patterns (Figure 6(a1–d3)). This regional heterogeneity manifested even synchronously, as exemplified by contrasting seasonal dynamics: at Xuliujing–South Branch (the block in Figure 7a), spatially averaged C_{TSM} measured 187 mg/L (summer, the orange curve in Figure 7b) versus 156 mg/L (autumn, the orange curve in Figure 7b), while the TMZ demonstrated an inverse pattern with significantly lower summer concentrations (Figure 6b,c). Furthermore, bathymetric control influenced the northwestern Zhoushan Archipelago sector, where deeper waters remained perennially enveloped by higher-C_{TSM} waters from Hangzhou Bay.

These monthly progression patterns align with established TSM transport regimes. Sun et al. [40] documented southward/eastward expansion of JAC-borne matters in November–March and nearshore contraction in May–September, with transitional phases in April and October. Our observed TSM front dynamics along the Jiangsu water (the block in Figure 7a)—exhibiting continued spreading through March and sustained contraction through September (Figure 6(a1–c1,d2))—demonstrate close consistency with this framework, which also confirms the reliability of the TSM data we reconstructed. Collectively, these spatio-temporal variations underscore that region-specific analysis is essential to resolve the complex TSM dynamics governing the Changjiang estuary–Hangzhou Bay system.

5. Discussion

5.1. Controlling Factors of TSM Concentration in Changjiang Estuary

TSM dynamics in the Changjiang estuary are governed by synergistic forcing mechanisms. The forcings impacting TSM dynamics, wind, tide, and current, are demonstrated in Figures 8–10 below.

The daily wind stress was selected from the hourly data between 16:00 the day before to 15:00 the satellite capturing day due to GOCI capturing time ending at 15:28 (the same to the tide and the resultant current data hereafter) and was averaged into the daily mean wind stress, and subsequently into the monthly mean wind stress in Figure 8.

The wind stress in the Zhoushan Archipelago region is remarkably intense throughout the year. The mean wind stress in 2020 was 0.272 N/m^2 in this region, where the wind stress exceeded 1 N/m^2 in some channels caused by the Venturi effect [41].

The resultant current about the Changjiang estuary in January and February exhibits a prevailing northward nearshore flow (Figure 10a,b). As a matter of fact, when studying the Changjiang plume characteristics, Wu et al. [42] argued that, even under the influence of northerly wind, the northward Changjiang plume can exist and transport to 34°N along the Jiangsu coast due to the spring tide. Furthermore, Kondo [43] also reported Changjiang runoff transport northeastward in winter. In Hangzhou Bay, an anticlockwise eddy was formed during March to July (Figure 10c–f). Zou et al. [44] reported that the northern branch of the TWC can flow to 30.5°N near the edge to Hangzhou Bay in winter. The branch of the TWC should be further intensified during March to May, when the dominant current nearshore is transferring to the TWC in spring [40] with the northerly wind weakened and

subsequently reversed in the bay. In the meantime, the anticlockwise circulation is also intensified by the tidal asymmetry [45]. Due to all the factors combined, the eddy lasted from March to July.

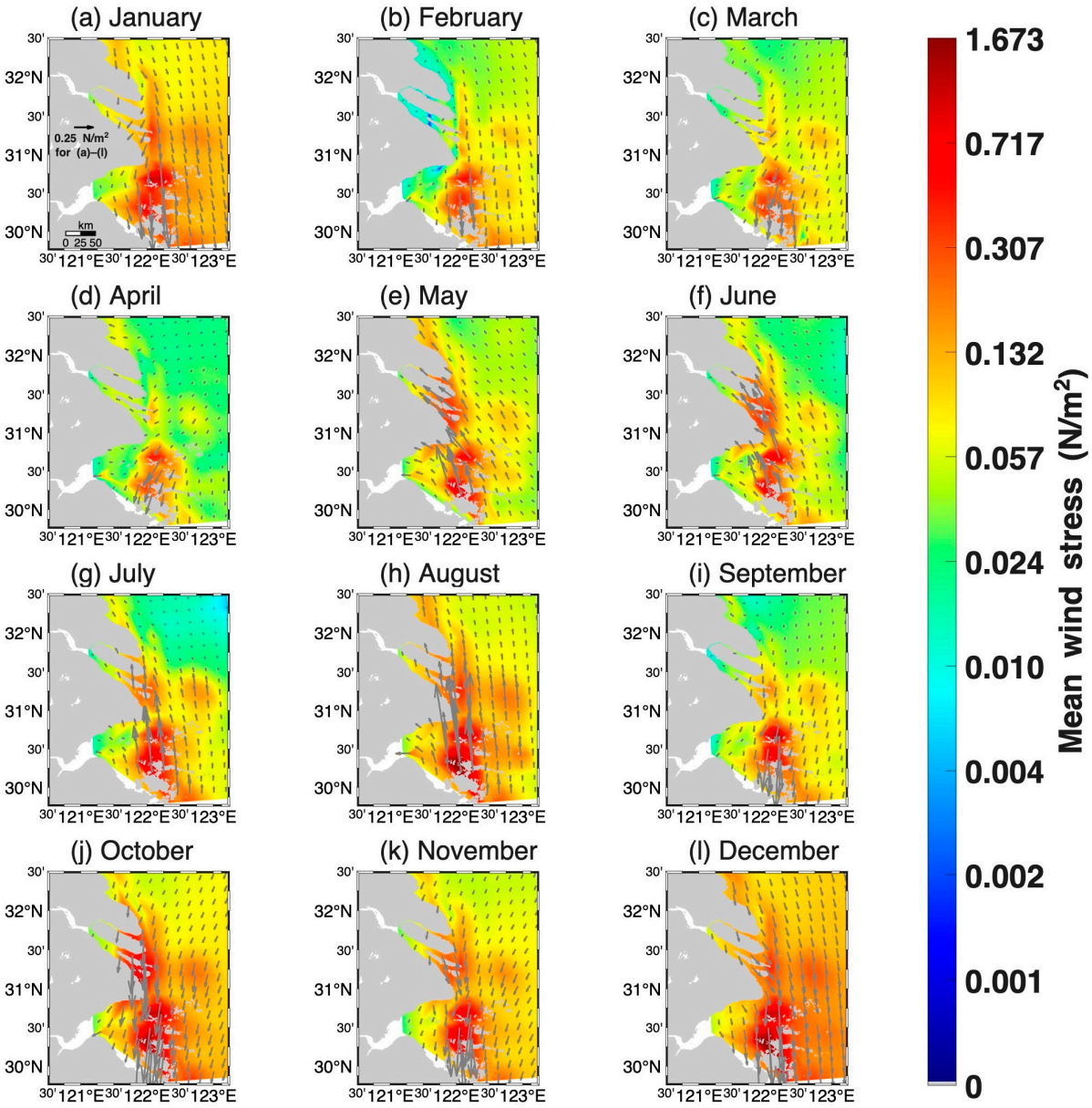

Figure 8. Monthly mean wind stress maps through the year of 2020. The colors denote the magnitude of wind stress. The directions of the arrows represent the directions of wind stress forcing and the lengths denote the magnitude of the wind stress vectors. The scale quiver for (**a**–**l**) is demonstrated in (**a**).

In the winter season, January's northerly monsoon dominance with geostrophic forcing inducing onshore flow (Figure 8a), and mean tidal currents transported southwestward along the Jiangsu coast (Figure 9a), the combined effect of which led to the resultant current field where the flow moved southwestward north to 32°N within the 10 m isobath (the Jiangsu water in Figure 7a), estuary-ward in the Changjiang estuary (Figure 10a). Moreover, the current transported clockwise near the Qidong shore, forming a circulation beyond the 10 m isobath that was ultimately transmitted into the estuary. This confluence elevated nearshore TSM of the Changjiang estuary and the Jiangsu coast to annual maxima (domain-averaged for the combined blocks of the Jiangsu water and the main estuary in Figure 7a:

410 mg/L) with spatially homogeneous distributions exhibiting north–south gradients (Figure 6(d1)). Hence, exceptionally high C_{TSM} in the TMZ arose from the resuspension caused by wind waves.

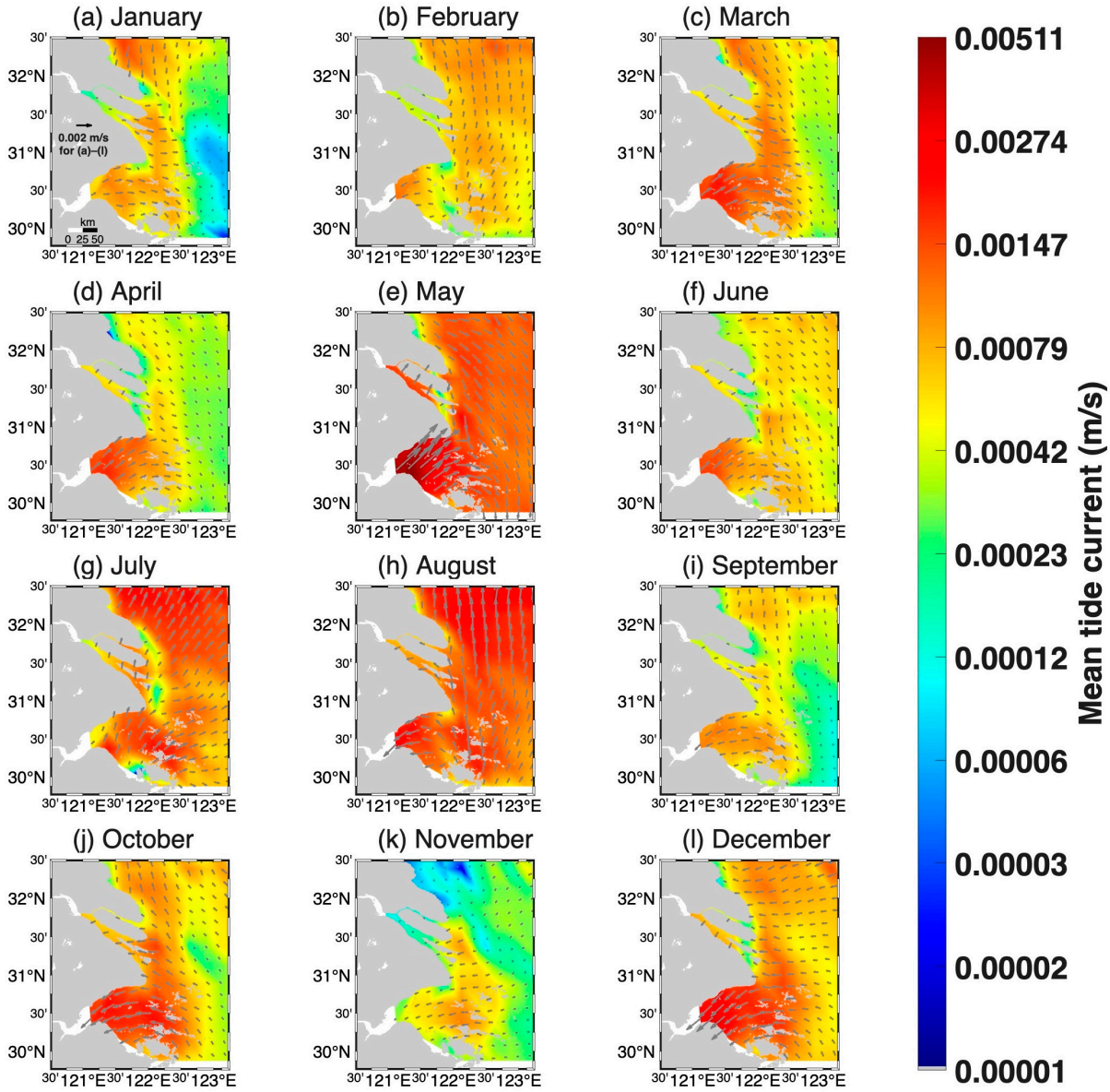

Figure 9. Monthly mean tide current maps through the year of 2020. The colors denote the magnitude of the mean tide current. The directions of the arrows represent the directions of the mean tide current and the lengths denote the magnitude of the mean tide current vectors. The scale quiver for (**a**–**l**) is demonstrated in (**a**).

By February, the northerlies (Figure 8b) weakened, which caused the resuspension to wane, triggering the C_{TSM} decline in the northern part of the study area (mean: 346 mg/L, for the combined blocks of the Jiangsu water and the main estuary). However, the mean tide currents transferred northward, causing the resultant current field a strengthened circulation (Figure 10b). Due to the disappearance of onshore flow along the Jiangsu coast, there was a turbid front stretching eastward. The current circulation formed a southward turbid path along 123°E. In addition, there was no current component transporting westward to the estuary from 123°E, leaving a clearer water band on 122.5°E. Hence, due to the dynamics of the resultant current and the weakened resuspension, the TSM in the TMZ declined in concentration and shrank in the front (Figure 6(d2)).

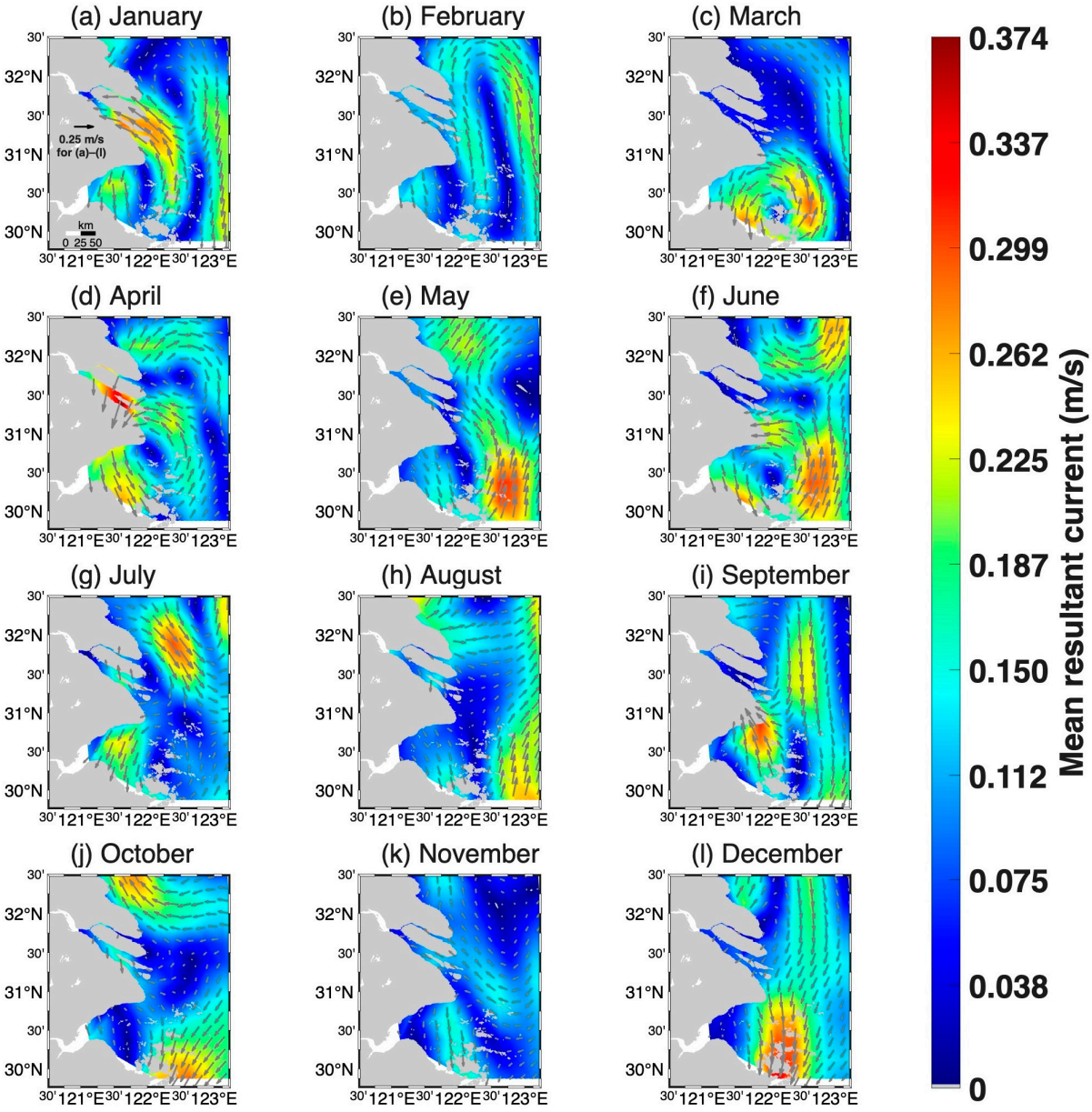

Figure 10. Monthly mean resultant current maps through the year of 2020. The term "resultant current" in this study refers to the current derived from the vector sum of the flows of tide, geostrophic flow, and Ekman drift. The colors denote the magnitude of the mean resultant current. The directions of the arrows represent the directions of the mean resultant current and the lengths denote the magnitude of the mean resultant current vectors. The scale quiver for (**a**–**l**) is demonstrated in (**a**).

For the purpose of analyzing the mechanisms of TSM transport dependent on current distribution, the current distribution in the more northward part of the Jiangsu coast (Figure 11a,b) and the TSM distribution where the locations A, B, and C were selected (Figure 11c,d), in January and February, respectively, are demonstrated below.

The statistical correlation coefficients among the three locations are summarized in Table 6, which follows Figure 11.

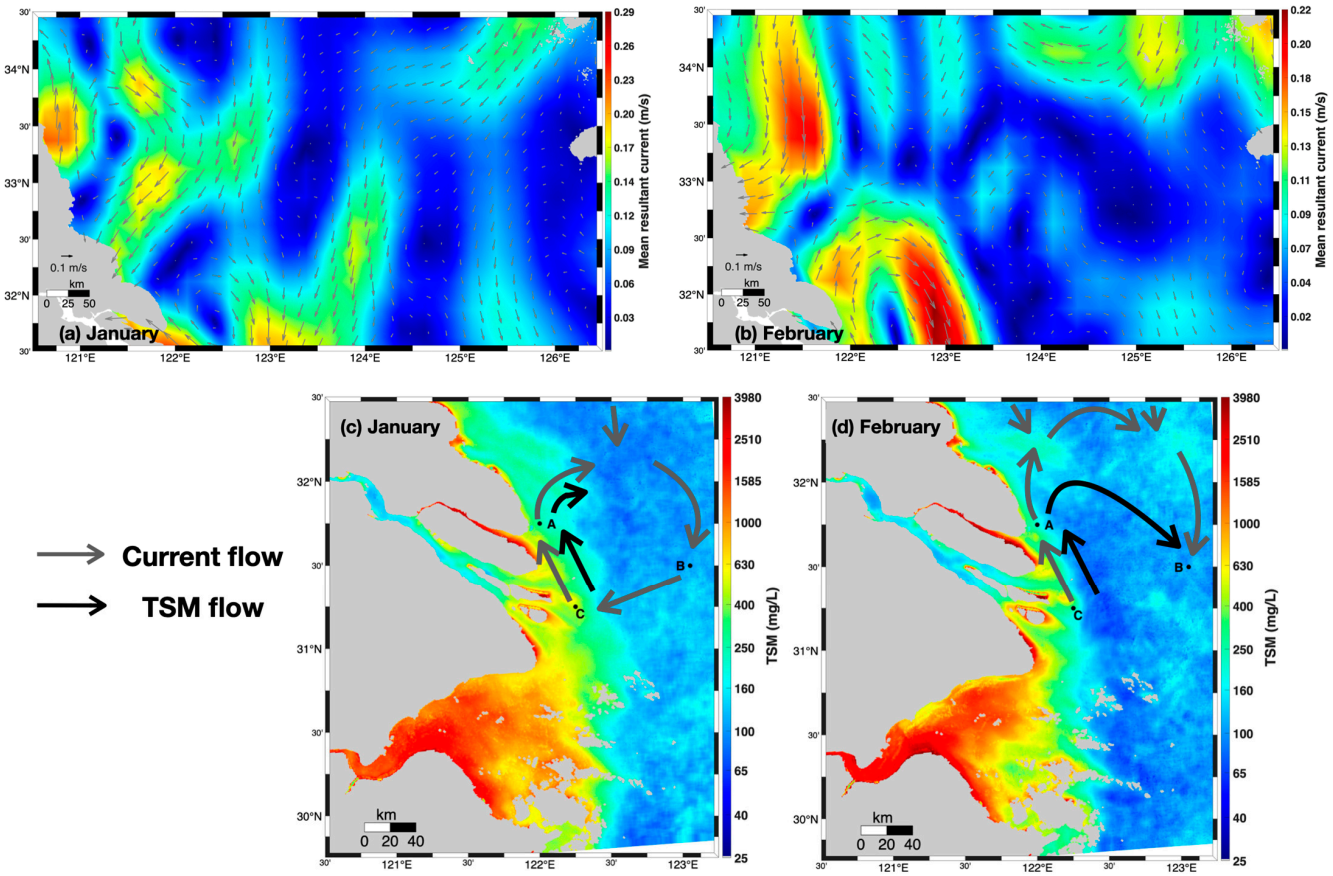

Figure 11. Monthly mean resultant current distribution in the region of 120.5°~126.5°E, 31.5°~34.5°N in (**a**) January and (**b**) February; TSM distribution in (**c**) January and (**d**) February. The dark gray arrows denote the current flows and the black arrows denote the TSM flows. The locations A, B, and C in (**c**,**d**) were selected to resolve TSM transport mechanisms.

Table 6. Statistical correlation coefficients of TSM and current among locations A, B, and C in January and February. The letter combinations for the table cells represent the coefficients between the specific locations (e.g., the cell AB for the coefficient between locations A, B). *p*-values of the coefficients displayed are less than 0.05. Cells of "\" denote no significant statistical correlation ($p > 0.05$ or coefficient absolute value < 0.3).

	TSM			**Current**		
Locations (January)	A	B	C	A	B	C
A	1	\	0.99	1	0.79	0.91
B	\	1	\	0.79	1	0.50
C	0.99	\	1	0.91	0.50	1
Locations (February)	A	B	C	A	B	C
A	1	0.84	0.92	1	−0.65	0.96
B	0.84	1	0.73	−0.65	1	−0.57
C	0.92	0.73	1	0.96	−0.57	1

The TSM and current exhibited much different transport characteristics in January, as Table 6 depicts. Locations A and C show the coefficient of high correlation (0.99) in TSM, with B showing no significant correlation with A or C. However, relating to the correlation in current, all the locations show coefficients revealing the current circulation

mechanism. As Figure 10a demonstrates, there is a clockwise circulation connecting A, B, and C, leading to a substantial coefficient of A and C at 0.91 (current-coefficient–A and C) and current-coefficient–A and B at 0.79. The absence of TSM-coefficient for B with either of A or C implies the deposition of TSM transporting from A to B and from B to C. As a matter of fact, the surface C_{TSM} can reduce to under 250 mg/L when the instant onshore current speed slows to 0.5 m/s or the instant offshore current speed slows to 1.5 m/s about the 10 m isobath in the Changjiang estuary and its adjacent seas [46]. Hence, the TSM transport routes from A to B and B to C were severed by deposition, as is in Figure 11c.

The current-coefficient of B and A, B and C turned minus in February; the current-coefficient–A and C kept high and positive, however. The current circulation about A, B, and C was impacted by the input of the JAC and Yellow Sea Warm Current (YSWC, 123°~124°E) [43] both in January and February, as Figure 11a,b reveals. However, different from the current field in January, there was scarcely a current transport between B and C to regulate the attributes of the currents in February, leading to the minus current-coefficients in Table 6, indicating that the stronger the current in A and C was, the stronger the resistance to the JAC and YSWC input was. Due to the stable and intense current conveyance from C via A then to B (Figure 10b), the C_{TSM} among A, B, and C resulted in good correlation.

Therefore, TSM plume transport is driven by current but does not definitely follow it, and the schematic transports of current and TSM in the two months are summarized in Figure 11c,d.

December maintained high C_{TSM} under strengthened northerlies and tides, where intensified resuspension and dominant southward flow eliminated Jiangsu's clear-water zones. The current field there (Figure 10l) was mainly controlled by the JAC, which carries high turbid water, yielding the TSM-coefficients of A and B, A and C, and B and C at 0.82, 0.99, and 0.76, respectively. Shen et al. [23] reported that the TSM of the Changjiang estuary is supplemented from the Jiangsu water, and the C_{TSM} near the estuary beyond the 10 m isobath is affected by the water mass of the Qidong shore in the winter. Combining the current and TSM circulation in winter, however, one can conclude that this supplement is conditional, which can be severed by local tide–wind effects.

Hence, tide and wind dominated the dynamics of C_{TSM} in the Changjiang estuary and the Jiangsu coast in winter, but it is the interactions of the currents (combined with JAC) that determine the transport of TSM.

In spring, March saw intensified wind stress amplifying its westward components (Figure 8c), yet the mean tide currents implied that the tide comprehensively transported southeastward in collision with the wind-driven flow in the east–west direction (Figure 9c). The resultant current map in Figure 10c indicates that the resultant current was more influenced by the tide current. As a result, the turbid front bent southeastward close to the coast in the Jiangsu water. Moreover, there was a significant estuary-ward flow in the southeast to the Chongming island, forming a turbid front conjunction between the onshore water and the offshore water (Figure 6(a1)), leading to the TSM-coefficient–B and C (the positions can be found in previous figures) there being 0.69.

April marked the TSM transport-retreat transition: the tidal weakening denoted by the mean tide current (Figure 9d) and the wind stress weakening (Figure 8d) precipitated a precipitous Jiangsu water TSM decline to 160–250 mg/L (mean: 188 mg/L, the blue curve in Figure 7b), while anomalous increases at the Xuliujing–South Branch (Figure 6(a2), the orange curve in Figure 7b) aligned with wind stress strengthening there and riverward flow restructuring in the TMZ. Concurrently, TSM fronts contracted and clear-water expanded westward with the clear water of the TWC transporting northward.

May's shift to southerlies combined with tide currents established northeastward offshore flow, allowing TWC penetration which capped Jiangsu water in clear water and

sharpened TMZ gradients. During this month, the TWC can be seen marching northward in the far southern region to the Zhoushan sea (Figure 12a), precipitating the waters south to the Zhoushan islands clear (Figure 12b). The moderate-to-high current-coefficients (Table 7) reveal that the TWC can transport to the region north to the Changjiang estuary and subsequently control TSM dynamics in D, C, and A, yielding high TSM-coefficients. The relating current and TSM routes are summarized in Figure 12b.

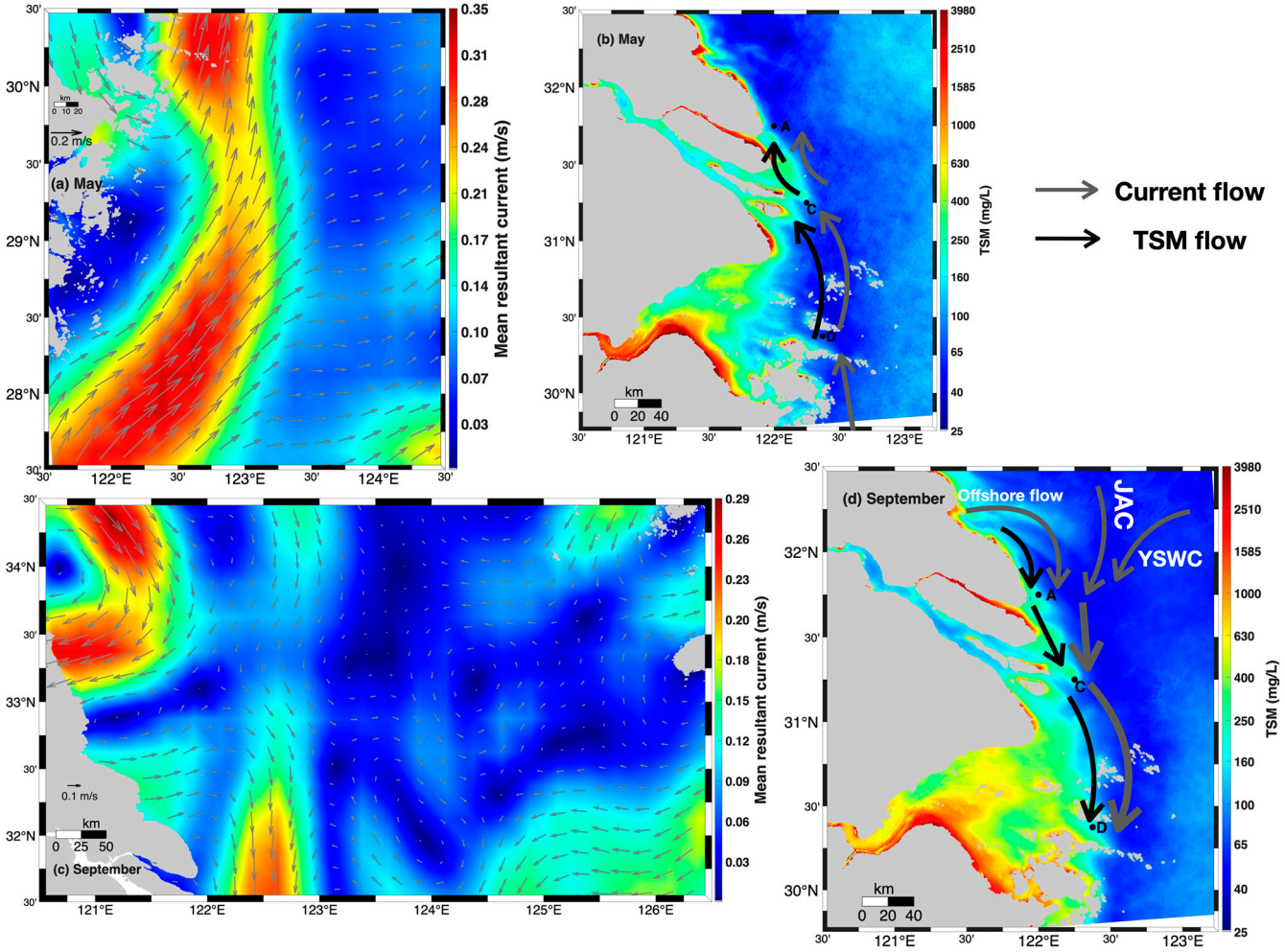

Figure 12. Monthly mean resultant current distribution in the region of 120.5°~124.5°E, 27.5°~30.5°N in (**a**) May and in the region of 120.5°~126.5°E, 31.5°~34.5°N in (**c**) September; TSM distribution in (**b**) May and (**d**) September. The dark gray arrows denote the current flows and the black arrows denote the TSM flows. The locations A, C, and D in (**b**,**d**) were selected to resolve TSM transport mechanisms.

In autumn, with the transition of the current field (TWC to JAC [40]) and September's returning northerlies (Figure 8i), the weakened offshore flow drove the turbid front to expand at the northern Jiangsu water (Figure 6(c1)). As Figure 12c shows, from 33° to 33.5°N along the Jiangsu coast, the JAC transports shoreward with one branch marching southward along 122.5°E. The wind–tide-induced offshore flow (32~32.5°N), the southward JAC branch, and the YSWC conveying clear water (Figure 12c, from east to 123°E, 31.5°N) together shaped the currents connecting A, C, and D (Figure 10i). The current-coefficients regarding the three locations are summarized in Table 7.

Table 7. Statistical correlation coefficients of TSM and current among locations A, C, and D in May and September. *p*-values of the coefficients displayed are less than 0.05. Cells of "\" denote no significant statistical correlation ($p > 0.05$ or coefficient absolute value < 0.3).

	TSM			**Current**		
Locations (May)	A	C	D	A	C	D
A	1	0.94	0.95	1	0.62	0.72
C	0.94	1	0.99	0.62	1	0.86
D	0.95	0.99	1	0.72	0.86	1
Locations (September)	A	C	D	A	C	D
A	1	0.96	0.74	1	\	−0.65
C	0.96	1	0.79	\	1	0.57
D	0.74	0.79	1	−0.65	0.57	1

From Figures 10i and 12d, it is clear that location A is in the scope of the influence of the wind–tide-induced offshore flow, while C and D are under the combined influence of the three flows (the bigger gray arrows) with the current-coefficient–C and D at 0.57. The current-coefficient–A and D at −0.65 indicates the competing status between the offshore flow and the background currents (JAC and YSWC). As a result, the TSM conveyed onshore by the JAC was then transported away from location A by the offshore flow, and subsequently spread along A to D through the combined flow, the process of which is revealed by the high TSM-correlation-coefficients among the locations at 0.96, 0.74, and 0.79, respectively, in Table 7. October's C_{TSM} increased further under the influence of the intensified wind stress and tide. November retained high C_{TSM} despite moderate forcing compared to October. The currents during the two months exhibited interesting distribution, as Figure 13 shows.

In October, the YSWC hampered the southward transport of the JAC to some extent (Figure 13a), where part of the JAC penetrated into the YSWC along 124°E and then bifurcated there westward and southward. The current distribution in Figure 10j implies that the TSM in location A and B should be correlated. As the evidence of this, the TSM-coefficient–A and B was at 0.69 with the TSM-coefficient–B and C of no statistical significance. In November, the southward JAC was totally severed at 33°N near the Jiangsu coast (Figure 13b); however, the YSWC transported southward carrying turbid water of Korea's southwestern coast [47] to the East China Sea and bent its way northwestward at 31°N due to the co-effect of tide and wind (Figure 10k), leading to the extended TSM front about the Jiangsu coast with lower gradients between the 10 m isobath and the outer sea compared to October. The TSM-coefficients of B and C, C and A, and B and A at 0.75, 0.96, and 0.68, respectively, imply the TSM path.

As the transitional seasons, spring and autumn share the shift in dominant monsoons and background circulation (TWC and JAC), when the shift characterized the distribution of turbid fronts with the contraction in spring and the expansion in autumn. However, the currents in autumn can be much more complex, when the interactions between the JAC and YSWC are significant.

Mid-summer (June and July) witnessed annual TSM minima (July mean C_{TSM} for the combined region of the Jiangsu water and the main estuary in Figure 7a: 173 mg/L) under peak Changjiang freshwater discharge (inducing stratification) and pervasive TWC influence (Figures 6(b1,b2) and 10f,g). Actually, the wind stress in the TMZ was not weak compared to that of April (Figure 8d,f,g), indicating that the stratification effect weakening resuspension and vertical mixing in water columns [23,48,49] of freshwater can weaken the

effect of wind forcing, which is consistent with the study of Geyer [50]. However, with the intrusion of the TWC in summer, the TSM dynamics are more complex compared to that under the sole influence of the Changjiang runoff stratification.

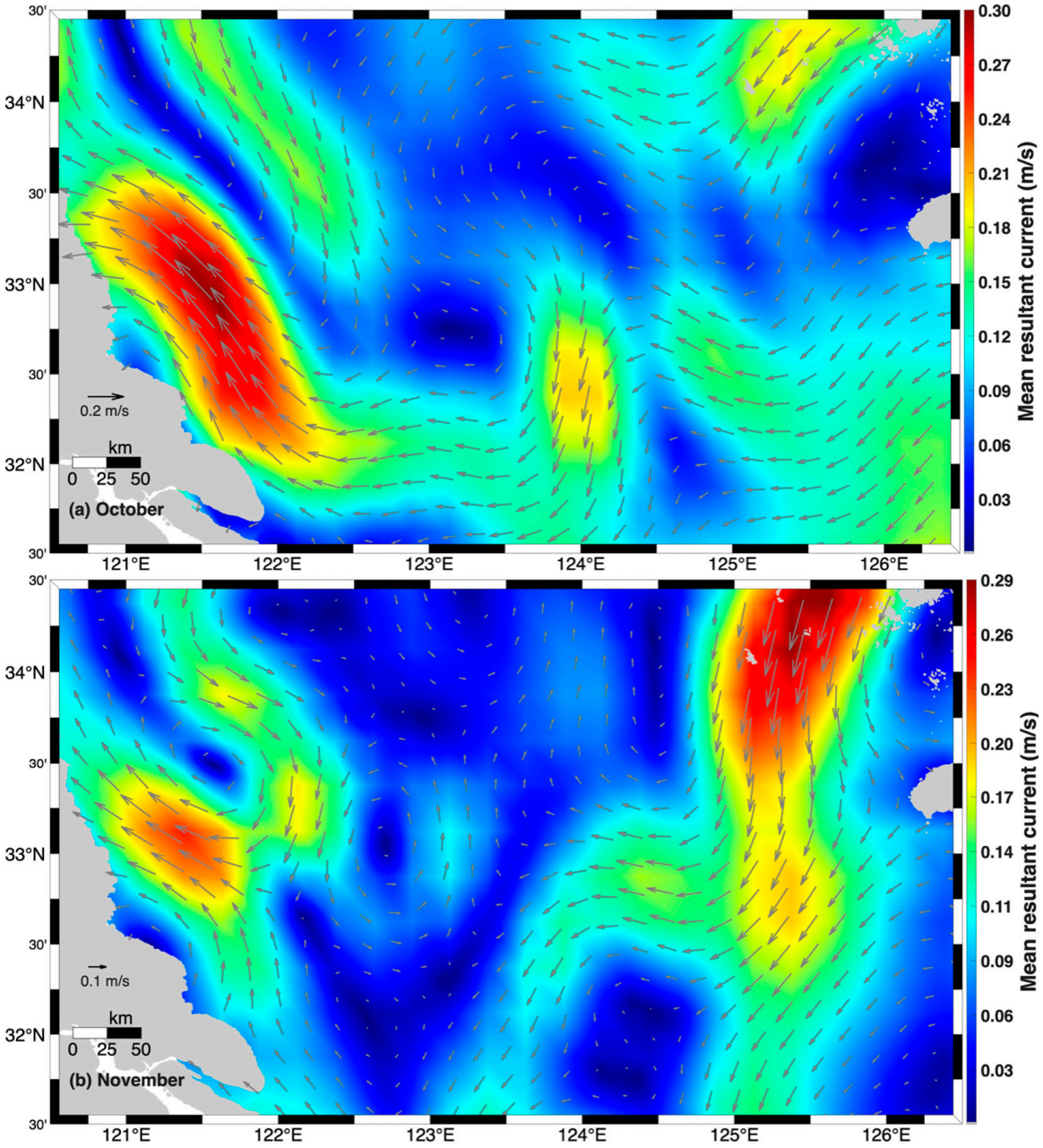

Figure 13. Mean current distribution of 120.5~126.5°E, 31.5°~34.5°N in (**a**) October and (**b**) November.

In Figure 14, the offshore flow generated about 32.75°N nearshore bent its way northward about 123°E, 32°N (Figure 14a) due to the co-driving of wind and tide. One branch of the TWC intruded into the Zhoushan water from the south with the currents from Hangzhou Bay merging there (Figure 14b). As a result, the two main flow circulations met along 31.25°N (Figure 14c), where the currents around interflowed about location C (denoted in Figure 14d).

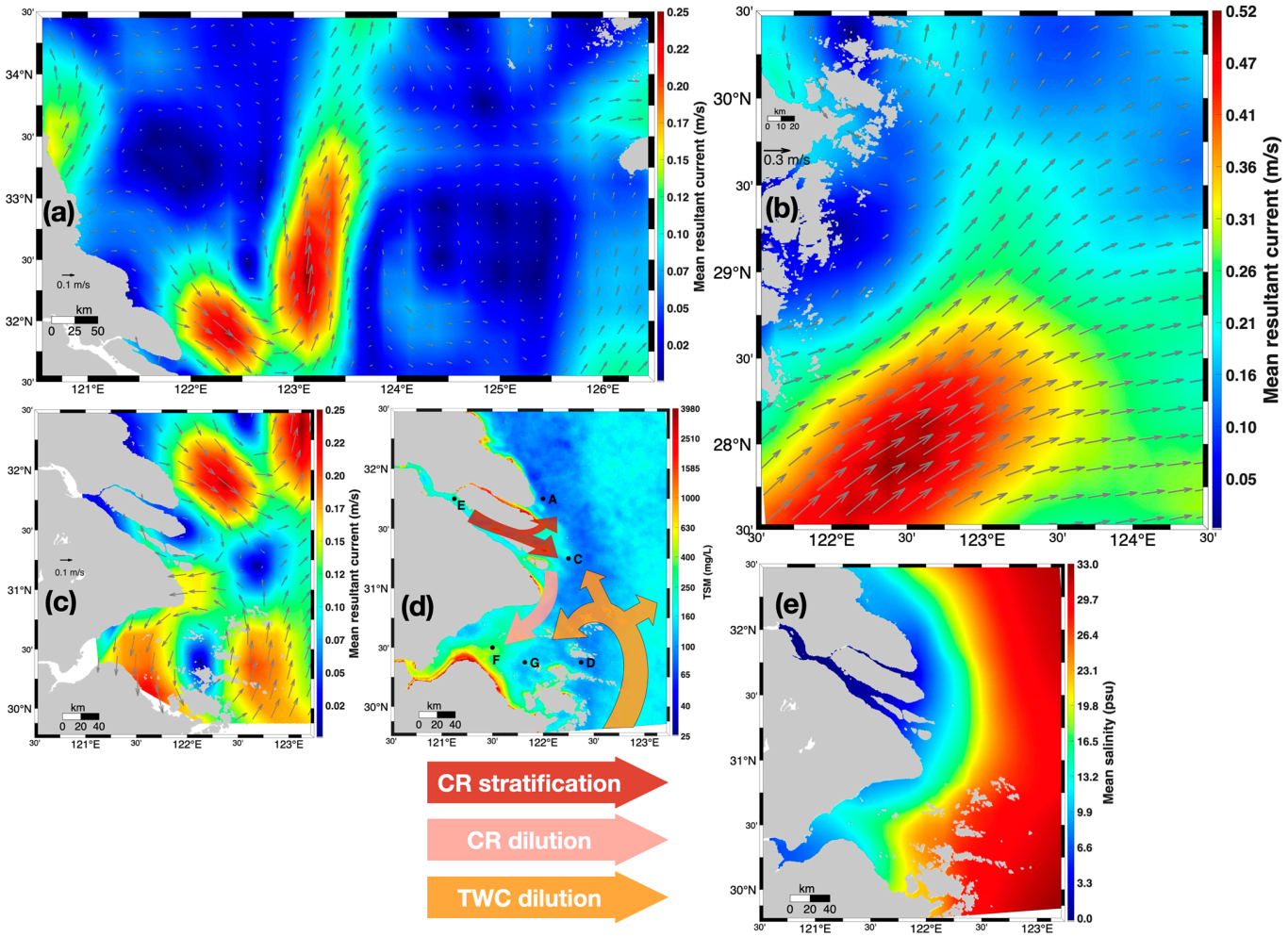

Figure 14. Mean resultant current distribution for June and July (**a**) in the region of 120.5°~126.5°E, 31.5°~34.5°N, (**b**) in the region of 120.5°~124.5°E, 27.5°~30.5°N, and (**c**) in the main study region. Mean TSM distribution for the two months is in (**d**) where the locations A, C, D, E, F and G were selected to resolve TSM transport mechanisms, the dark red arrows represent the Changjiang runoff (CR) stratification, the light red arrow the CR dilution, and the orange arrows the TWC dilution. Mean salinity distribution is in (**e**).

The TSM in Xuliujing (location E, Figure 14d) is dominated by the Changjiang runoff, where, generally, the larger runoff magnitude leads to the higher C_{TSM} [23]. The TSM-coefficients of E with A or C exhibited no significant statistical relation. The study of Li et al. [48] argued that the stratification inhibiting vertical mixing traps the TSM in the stratified bottom layer in the TMZ (where location C lies). However, TSM-coefficient–E and F was at −0.55, indicating the significant runoff dilution there after TSM being trapped in the TMZ. Wei et al. [51] reported that the Changjiang runoff can largely intrude into Hangzhou Bay against the summer southerly monsoon driven by Changjiang discharge, intraseasonal winds, tidal residual currents, etc., the intrusion of which is greater in summer than in winter, causing unique low-salinity water mass in the north-central bay, as shown in Figure 14e.

With respect to the TWC, the TSM-coefficients of D with C, F, and G were at 0.48, 0.21 (with $p > 0.05$), and 0.79, respectively. Therefore, the TSM in the TMZ was significantly impacted by the co-effect of the runoff stratification and the TWC dilution; within the 10 m isobath (where location F lies), the Changjiang runoff dilution effect overweighed that of the TWC. However, the TWC dilution surpassed the Changjiang runoff dilution

(TSM-coefficient–E and G at −0.1, $p > 0.05$, which was negligible) beyond the 10 m isobath. The schematic interactions of the Changjiang runoff (CR) and the TWC are summarized in Figure 14d.

The wind-induced eastward/southeastward offshore flow in August resisted the intrusion of the TWC (Figure 10h). As a result, neither the TSM-coefficient–B and D nor current-coefficient–B and D shows a significant statistical correlation. Strengthened wind and tide forcing compared that of July increased the C_{TSM} in the TMZ (Figure 6(b3)).

In conclusion, C_{TSM} in summertime hits the nadir compared to other seasons when the stratification and the dilution become dominant.

5.2. Controlling Factors of TSM Concentration in Hangzhou Bay

In winter, January–February northerlies coupled with strong west-bay-intensifying tides generated southward-convergent flows (Figure 10a,b), sustaining west-high C_{TSM} gradients fueled by Changjiang sediment inputs (Figure 6(d1,d2)), with TSM-coefficient–E and F at 0.92 and 0.87 for January and February, respectively. During the two months, one part of the currents discharging out of Hangzhou Bay from the south interflowed with the southward JAC, while the other part transported northward through the archipelago, colliding with the JAC and resulting in the low-speed zone east to the archipelago (Figure 15a,b).

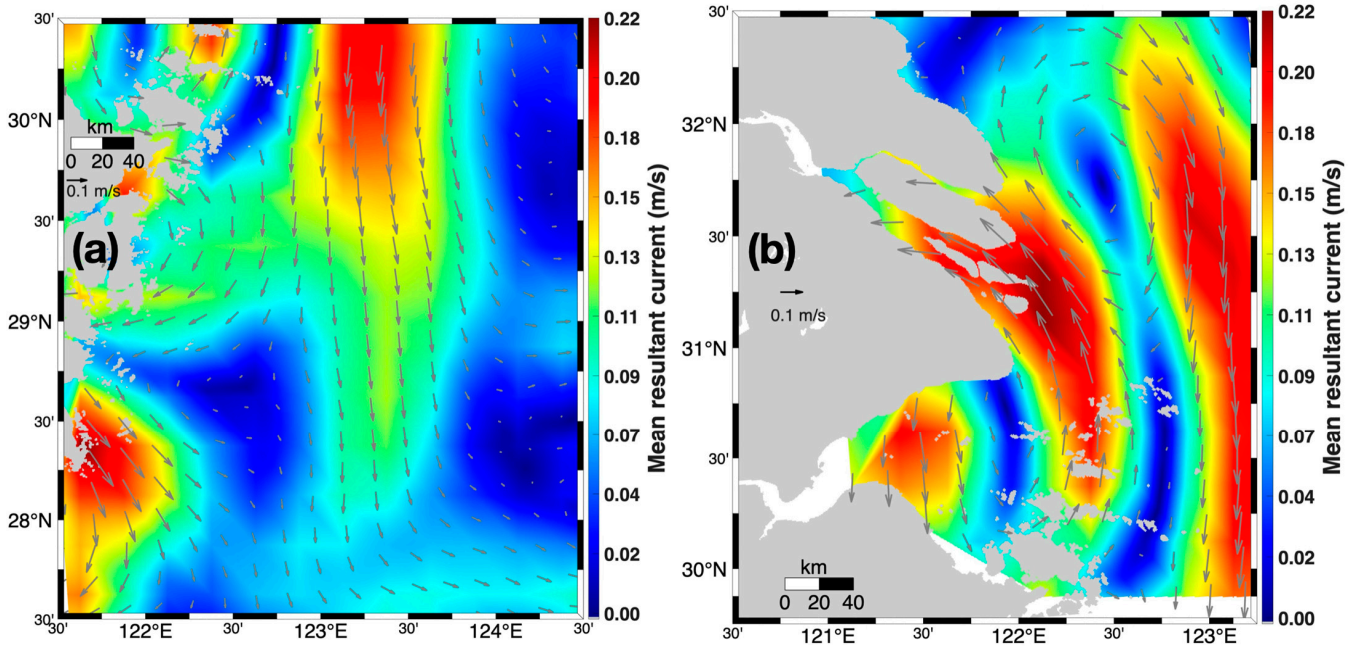

Figure 15. Mean current distribution in January and February for (**a**) the region south of the study region and for (**b**) the study region.

TSM-coefficient–F and D and current-coefficient–F and D during the two months were at 0.62 and 0.51, respectively. A numerical study run for winter and early spring indicates that an anticlockwise flow is formed by tidal asymmetry and the current speed is large at the mouth and the head of the bay due to the islands and the narrow channel [45]. It can be seen that the impact of this circulation can reach the TMZ (Figure 15b), with TSM-coefficient–D and C and current-coefficient–D and C at 0.82 and 0.93, respectively.

The wind stress was significantly more intense in December than in January and February, shaping the southward currents. However, December's elevated northerlies and intense tides yielded paradoxical TSM declines (Figure 6(d3))—potentially indicating cloud-scattering artifacts—meriting further investigation given satellite data discrepancies.

In spring, March maintained the pattern of that in January and February (Figure 6(a1); mean value of Hangzhou Bay: 861 mg/L, the purple curve in Figure 7b) when the turbid plume was contracted westward due to the TWC starting to intrude from the south, as Figure 16 depicts.

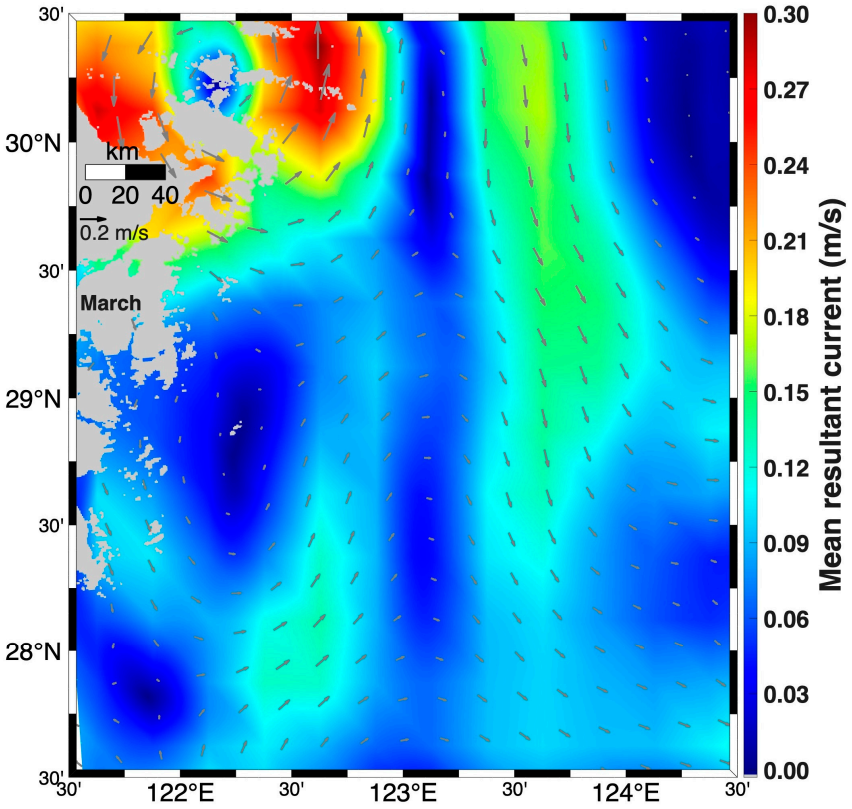

Figure 16. Mean current distribution in March for the region south to the study region.

April's tidal collapse triggered a system-wide TSM decline (mean: 487 mg/L, the purple curve in Figure 7b), retreating high values in the southern bay as the TWC [40,44] was diluting the bay more strongly (Figures 6(a2) and 10d). May juxtaposed both enhanced southerlies and tides: wind-induced resuspension elevated TSM along shallow southern banks (e.g., Andong), while the TWC cleared waters east of 121.75°E (Figures 6(a3) and 12b).

In autumn, September's established northerlies and tides drove a further TSM rise (Figures 8i and 9i), saturating the bay (Figure 6(c1)). Due to the intensity zone of wind stress (in the archipelago) and mean tide current (the sea south to Shanghai) located allopatrically, the currents converged northeast to Hangzhou Bay, which led to a Shanghai–Andong surface TSM band. Due to the scarce existence of west–east currents between the inner and the outer sea, the YSWC (Figure 12c) transport caused a clear-water zone out of the bay along 122.5°E. October intensified northeasterlies/northerlies with vigorous tides (Figures 8j and 9j), establishing dual wind–tide control while expanding southward TSM inputs (Figure 6(c2)). November's resultant currents in the bay propelled high C_{TSM} fronts past the Zhoushan Archipelago (Figures 10k and 6(c3)), achieving late-year concentration maxima, where the TSM-coefficients among locations F, G, and D were greater than 0.95.

In Summertime, June–July represented the annual TSM nadir (Figure 6(b1,b2)) under the TWC and the Changjiang runoff dilution (Figure 14d) that competed in the proximity of location G, as discussed in Section 5.1. August marked the reversal: synergistic southerly winds and resurgent tides restored TSM (Figures 6(b3), 8h and 9h), expanding TSM fronts eastward as the TWC was expelled eastward by the bay offshore flow. Location D, which lies

on the boundary between the two competing flows, showed no statistical correlations with G over current; however, TSM-coefficient–D and G was at 0.98 with TSM-coefficient–F and G at 0.82, indicating that wind and tide in the bay reclaimed the control of TSM dynamics.

6. Conclusions

This study developed an improved TSM retrieval algorithm for the Changjiang estuary–Hangzhou Bay region using expanded training and validation datasets, enhancing accuracy and generalizability. The DINEOF method was leveraged to mitigate cloud-induced data gaps, resulting in a continuous high-resolution TSM dataset that enabled detailed analysis of spatio-temporal dynamics and underlying mechanisms.

Based on the new high-resolution TSM dataset, we clarified the coastal TSM spatio-temporal dynamics: dry-season high C_{TSM} in the Changjiang estuary and Jiangsu water is sustained by tide–wind resuspension and southward transport of JAC-borne TSM. Notably, under the influence of the clockwise nearshore circulation from the Changjiang estuary to the Jiangsu water, the Jiangsu-origin surface TSM can transport to the outer sea without supplementing the TSM in the TMZ, which indicates that the model that "dry-season TSM in the Changjiang estuary is supplemented by the Jiangsu water" is conditional. Wet-season conditions feature low C_{TSM}, with the Changjiang runoff stratification in the Qidong water and TMZ and the dilution of the Changjiang runoff and TWC in Hangzhou Bay.

Meanwhile, this study identified the controlling mechanisms of TSM dynamics: dry-season TSM elevations are attributed to wind–tide resuspension and JAC-mediated transport. Northerly winds drive resuspension and plume formation along the Jiangsu coast, with subsequent delivery and local resuspension elevating TSM in the TMZ. However, whether carrying the turbid water from the Korean southwestern coast, the YSWC can cause high nearshore C_{TSM} gradients in September or low nearshore C_{TSM} gradients in November. The JAC, YSWC, and wind–tide-induced currents constitute the complex background current system in dry season. Wet-season reductions arise from TWC intrusion compounded by stratification that dampens resuspension and dilution from Changjiang discharge. Hangzhou Bay's unique topography facilitates tide–wind resuspension maintaining high TSM, though wet-season dilution by TWC and the Changjiang runoff reduces concentrations.

While DINEOFs effectively addressed cloud cover gaps, residual cloud-scattering artifacts may influence data quality, as suggested by discrepancies between buoy measurements (November: 199 mg/L; December: 295 mg/L) and satellite-derived December values. Specifically, cloud adjacency effects and sub-pixel cloud contamination can lead to the over-correction of atmospheric path radiance, resulting in an underestimation of retrieved TSM concentrations in partially cloudy or hazy conditions. Such artifacts are particularly pronounced in highly turbid and dynamically variable waters like the Changjiang estuary, where aerosol and hydrosol properties change rapidly in time and space. The observed discrepancy in December—a month characterized by strong northerly winds and enhanced resuspension—highlights the need to further discriminate between true sediment-driven turbidity and cloud-induced radiometric noise. This issue underscores the necessity for the continued refinement of atmospheric correction methods tailored to turbid coastal environments, as well as the integration of multi-sensor (e.g., SAR, lidar) and multi-temporal approaches to validate and complement optical remote sensing products under non-ideal atmospheric conditions.

Author Contributions: Conceptualization, Y.Y. and Y.L.; methodology, Z.T., Y.Y. and Y.L.; software, Z.T.; validation, Z.T., Y.Y. and S.H.; formal analysis, Z.T.; investigation, Z.T.; resources, S.H. and Y.Y.; data curation, Z.T.; writing—original draft preparation, Z.T.; writing—review and editing, Z.T., S.H. and Y.Y.; visualization, Z.T.; supervision, Y.Y. and Y.L.; project administration, Y.Y., S.H. and

Y.L.; funding acquisition, S.H. and Y.Y. All authors have read and agreed to the published version of the manuscript.

Funding: This research was supported by National Natural Science Foundation of China (Nos. 42576185 and 42576004), and Zhejiang Provincial Natural Science Foundation of China (No. LD24D060002).

Data Availability Statement: GOCI, wind, tide, current and salinity data sets are publicly available from corresponding agencies: GOCI satellite data from the Korea Ocean Satellite Center (KOSC, https://kosc.kiost.ac.kr/, accessed on 9 December 2024), wind, tide, current and salinity data from the Copernicus Marine Data Store (CMDS, https://data.marine.copernicus.eu/, accessed on 14 April 2025). Changjiang river runoff data were provided by courtesy of Bureau of Hydrology, Changjiang Water Resources Commission, Ministry of Water Resources, People's Republic of China. The other dataset that supports the findings of this study is available from the corresponding author upon request.

Conflicts of Interest: The authors declare no conflicts of interest.

References

1. Cloern, J.E. Turbidity as a control on phytoplankton biomass and productivity in estuaries. *Cont. Shelf Res.* **1987**, *7*, 1367–1381. [CrossRef]
2. Winter, D.F.; Banse, K.; Anderson, G.C. The dynamics of phytoplankton blooms in puget sound a fjord in the Northwestern United States. *Mar. Biol.* **1975**, *29*, 139–176. [CrossRef]
3. Miller, R.L.; Cruise, J.F. Effects of suspended sediments on coral growth—Evidence from remote-sensing and hydrologic modeling. *Remote Sens. Environ.* **1995**, *53*, 177–187. [CrossRef]
4. Hudson, J.H. Growth rates in Montastraea annularis: A record of environmental change in Key Largo Coral Reef Marine Sanctuary, Florida. *Bull. Mar. Sci.* **1981**, *31*, 444–459. [CrossRef]
5. Smith, S.V.; Hollibaugh, J.T. Coastal metabolism and the oceanic organic carbon balance. *Rev. Geophys.* **1993**, *31*, 75–89. [CrossRef]
6. Smith, S.V.; Mackenzie, F.T. The ocean as a net heterotrophic system: Implications from the carbon biogeochemical cycle. *Glob. Biogeochem. Cycles* **1987**, *1*, 187–198. [CrossRef]
7. Mayer, L.M.; Keil, R.G.; Macko, S.A.; Joye, S.B.; Ruttenberg, K.C.; Aller, R.C. Importance of suspended participates in riverine delivery of bioavailable nitrogen to coastal zones. *Glob. Biogeochem. Cycles* **1998**, *12*, 573–579. [CrossRef]
8. Du, P. Sediment Transport Research in Yangtze Estuary and Hangzhou Bay. Ph.D. Thesis, East China Normal University, Shanghai, China, 2007. Available online: https://kns.cnki.net/kcms2/article/abstract?v=Mw9fkKjKljqY72h7vSRXc6eJEygY8g-ymJqIcMDFk8hlUFAByB2O1A1YCH77lNSz2xR9tSHNd9YBlugeAw-3YVfVy22NIl2zrd86l1T7hzEcVxl8YtaaGbBUMnrifHobxsOBBh6A8PMkW08A8oGtiY3rqt7DcEj-ZBVAgRQuR8QSX5gSypQfc-bhFNSXDN0FnBSb2dPQ6jg=&uniplatform=NZKPT&language=CHS (accessed on 7 April 2022).
9. Ye, T. The Multi-Scale Variations of Suspended Sediment Dynamics in Hangzhou Bay and Its Interaction with Tidal Flat Variations. Master's Thesis, Zhejiang University, Hangzhou, China, 2019. Available online: https://kns.cnki.net/kcms2/article/abstract?v=Mw9fkKjKljo77dc4xencO75j8STvfu8uLk6VoO0JjNSNjBWoQB_IlT9V147ZdV9BiMYy0Gj7NNp9nwvn8OUhUIVaNPOqkv3T058tPw6mzYyvyqsLU5hfRxRAIO9ufGYIHRYfLgpqzfIPgtJC6VEIC52SCWaOjxkjEClIsP_WAwVbn-M72rvjTTtSlvM2kdf7ytJNIHOQmWY=&uniplatform=NZKPT&language=CHS (accessed on 15 October 2021).
10. Pan, C.H.; Zeng, J.; Tang, Z.W.; Shi, Y.B. Study on sediment characteristics and riverbed erosion and deposition at the mouth of Qiantang River. *Hydro-Sci. Eng.* **2013**, 1–7. [CrossRef]
11. Che, Y.; He, Q.; Lin, W.Q. The distributions of particulate heavy metals and its indication to the transfer of sediments in the Changjiang Estuary and Hangzhou Bay, China. *Mar. Pollut. Bull.* **2003**, *46*, 123–131. [CrossRef]
12. Guo, M.; Li, X.; Song, C.; Liu, G.; Zhou, Y. Photo-induced phosphate release during sediment resuspension in shallow lakes: A potential positive feedback mechanism of eutrophication. *Environ. Pollut.* **2020**, *258*, 113679. [CrossRef]
13. He, X.Q.; Bai, Y.; Pan, D.L.; Tang, J.W.; Wang, D.F. Atmospheric correction of satellite ocean color imagery using the ultraviolet wavelength for highly turbid waters. *Opt. Express* **2012**, *20*, 20754–20770. [CrossRef]
14. He, X.Q.; Bai, Y.; Pan, D.L.; Huang, N.L.; Dong, X.; Chen, J.S.; Chen, C.T.A.; Cui, Q.F. Using geostationary satellite ocean color data to map the diurnal dynamics of suspended particulate matter in coastal waters. *Remote Sens. Environ.* **2013**, *133*, 225–239. [CrossRef]
15. Hu, Y.K.; Yu, Z.F.; Zhou, B.; Li, Y.; Yin, S.J.; He, X.Q.; Peng, X.X.; Shum, C.K. Tidal-driven variation of suspended sediment in Hangzhou Bay based on GOCI data. *Int. J. Appl. Earth Obs.* **2019**, *82*, 101920–101932. [CrossRef]

16. Du, Y.; Lin, H.; He, S.; Wang, D.; Wang, Y.; Zhang, J. Tide-induced variability and mechanisms of surface suspended sediment in the Zhoushan Archipelago along the southeastern coast of China based on GOCI data. *Remote Sens.* **2021**, *13*, 929. [CrossRef]
17. Ma, Z.Y.; Zhao, Y.; Zhao, W.J.; Feng, J.J.; Liu, Y.Y.; Tsou, J.Y.; Zhang, Y.Z. Estimating total suspended matter and analyzing influencing factors in the Pearl River Estuary (China). *J. Mar. Sci. Eng.* **2024**, *12*, 167. [CrossRef]
18. He, M.; He, S.; Lu, S.; Gu, Y.; Zhou, F.; Ni, X.; Zhu, C.; Li, P. A simple and effective algorithm to retrieve total suspended matter from GOCI data in Hangzhou Bay, China. *Sci. Total Environ.* **2025**, *969*, 178903. [CrossRef] [PubMed]
19. Milliman, J.D.; Hsueh, Y.; Hu, D.X.; Pashinski, D.J.; Shen, H.T. Tidal phase control of sediment discharge from the Yangtze River. *Estuar. Coast. Shelf Sci.* **1984**, *19*, 119–128. [CrossRef]
20. Yang, Z.; Lei, K.; Guo, Z.; Wang, H. Effect of a winter storm on sediment transport and resuspension in the distal mud area, the East China Sea. *J. Coast. Res.* **2007**, *23*, 310–318. [CrossRef]
21. Zhou, Y.; Xuan, J.L.; Huang, D.J. Tidal variation of total suspended solids over the Yangtze Bank based on the geostationary ocean color imager. *Sci. China Earth Sci.* **2020**, *63*, 1381–1389. [CrossRef]
22. Chen, R.R.; Jiang, X.Z. Analysis of suspended sediment variations from the Yangtze Estuary to Zhejiang-Fujian Provincial coastal waters using remotely sensed data. *Mar. Sci.* **2017**, *41*, 89–101.
23. Shen, F.; Zhou, Y.X.; Li, J.F.; He, Q.; Verhoef, W. Remotely sensed variability of the suspended sediment concentration and its response to decreased river discharge in the Yangtze estuary and adjacent coast. *Cont. Shelf Res.* **2013**, *69*, 52–61. [CrossRef]
24. Du, P.; Ding, P.; Hu, K. Simulation of three-dimensional cohesive sediment transport in Hangzhou Bay, China. *Acta Oceanol. Sin.* **2010**, *29*, 98–106. [CrossRef]
25. Li, P.; Yang, S.L.; Milliman, J.D.; Xu, K.H.; Qin, W.H.; Wu, C.S.; Chen, Y.P.; Shi, B.W. Spatial, temporal, and human-induced variations in suspended sediment concentration in the surface waters of the Yangtze estuary and adjacent coastal areas. *Estuaries Coasts* **2012**, *35*, 1316–1327. [CrossRef]
26. Limeburner, R.; Beardsley, R.C.; Zhao, J.S. Water masses and circulation in the East China Sea. In Proceedings of the International Symposium on Sedimentation on the Continental Shelf, with Special Reference to the East China Sea, Hangzhou, China, 12–16 April 1983; pp. 285–294.
27. Su, J.L.; Wang, K.S. Changjiang river plume and suspended sediment transport in Hangzhou Bay. *Cont. Shelf Res.* **1989**, *9*, 93–111. [CrossRef]
28. Yuan, D.L.; Zhu, J.R.; Li, C.Y.; Hu, D.X. Cross-shelf circulation in the Yellow and East China Seas indicated by MODIS satellite observations. *J. Mar. Syst.* **2008**, *70*, 134–149. [CrossRef]
29. Li, J.F.; Zhang, C. Sediment resuspension and implications for turbidity maximum in the Changjiang Estuary. *Mar. Geol.* **1998**, *148*, 117–124. [CrossRef]
30. Shen, H.T.; Li, J.F.; Han, M.B. Transport of the suspended sediment in the Changjiang Estuary. *Int. J. Sediment Res.* **1992**, *7*, 45–63.
31. Shi, W.R.; Li, J.F. Mud transport calculation in Yangtse estuary and analysis of formation of turbidity maximum. *Mar. Sci. Bull.* **1993**, *12*, 69–76.
32. Wu, H.L.; Shen, H.T.; Yan, Y.X.; Wang, Y.H. Preliminary study on sediment flux into the sela from Changjiang Estuary. *J. Sediment Res.* **2006**, *6*, 75–81. [CrossRef]
33. Wang, B.C.; Eisma, D. Supply and deposition of sediment along the north bank of Hangzhou Bay, China. *Neth. J. Sea Res.* **1990**, *25*, 377–390. [CrossRef]
34. Zhao, J.; He, Q.; Wang, X.Y.; Guo, L.C. Field observations on the characteristics of current and sediment of the south and north branches in the Yangtze estuary. *Resour. Environ. Yangtze Basin* **2015**, *24*, 21–29. [CrossRef]
35. Tang, R.; Shen, F.; Pan, Y.; Liu, K.; Li, M.; Gao, W.; Zang, C. Cross-comparison of ocean color products derived from Tiangong-2/WIS and GOCI in the Yangtze estuary, China. In Proceedings of the Tiangong-2 Remote Sensing Application Conference, Beijing, China, 8 December 2018; Springer: Singapore, 2019; pp. 201–211. [CrossRef]
36. Tang, R.G.; Shen, F.; Pan, Y.Q.; Ruddick, K.; Shang, P. Multi-source high-resolution satellite products in Yangtze Estuary: Cross-comparisons and impacts of signal-to-noise ratio and spatial resolution. *Opt. Express* **2019**, *27*, 6426–6441. [CrossRef]
37. Liu, J.; Liu, J.H.; He, X.Q.; Pan, D.L.; Bai, Y.; Zhu, F.; Chen, T.Q.; Wang, Y.H. Diurnal dynamics and seasonal variations of total suspended particulate matter in highly turbid Hangzhou Bay waters based on the Geostationary Ocean Color Imager. *IEEE J. Sel. Top. Appl. Earth Obs. Remote Sens.* **2018**, *11*, 2170–2180. [CrossRef]
38. Gordon, H.R.; Voss, K.J. *MODIS Normalized Water-Leaving Radiance Algorithm Theoretical Basis Document (MOD 18) Version 4; NASA Contract Number NAS503163*; University of Miami: Coral Gables, FL, USA, 1999; pp. 1–96.
39. Tanaka, Y.; Inn, E.C.Y.; Watanabe, K. Absorption coefficients of gases in the vacuum ultraviolet. Part IV. Ozone. *J. Chem. Phys.* **1953**, *21*, 1651–1653. [CrossRef]
40. Sun, X.; Fang, M.; Huang, W. Spatial and temporal variations in suspended particulate matter transport on the Yellow and East China Sea shelf. *Oceanol. Limnol. Sin.* **2000**, *31*, 581–587. [CrossRef]
41. Xue, L.; Li, Y.; Xu, Y.; Wang, L.; Dai, G. Effect of Taiwan topography on the rapid intensification of typhoon Meranti (1010) passing by the Taiwan Strait. *Chin. J. Atmos. Sci.* **2015**, *39*, 789–801.

42. Wu, H.; Shen, J.; Zhu, J.; Zhang, J.; Li, L. Characteristics of the Changjiang plume and its extension along the Jiangsu Coast. *Cont. Shelf Res.* **2014**, *76*, 108–123. [CrossRef]
43. Kondo, M. Oceanographic investigations of fishing grounds in the East China Sea and the Yellow Sea-I. Characteristics of the mean temperature and salinity distributions measured at 50m and near the bottom. *Bull. Seikai Reg. Fish. Res. Lab.* **1985**, *62*, 19–66.
44. Zou, T.; Liu, Z.; Gao, H.; Sun, W. Simulations of Lagrangian residual current in Changjiang Estuary, Hangzhou Bay and their adjacent area. In Proceedings of the 2009 3rd International Conference on Bioinformatics and Biomedical Engineering, Beijing, China, 11–13 June 2009; pp. 1–3. [CrossRef]
45. Li, L.; Wu, L.; Chen, X.; Ren, Y.; Ye, T.; Yang, M.; Zhao, X. Asymmetric tidal dynamics in the macro-tidal Hangzhou Bay, China. *Estuaries Coasts* **2024**, *47*, 1418–1434. [CrossRef]
46. Milliman, J.D.; Shen, H.T.; Yang, Z.S.; Mead, R.H. Transport and deposition of river sediment in the Changjiang estuary and adjacent continental shelf. *Cont. Shelf Res.* **1985**, *4*, 37–45. [CrossRef]
47. Choi, J.K.; Park, Y.J.; Ahn, J.H.; Lim, H.S.; Eom, J.; Ryu, J.H. GOCI, the world's first geostationary ocean color observation satellite, for the monitoring of temporal variability in coastal water turbidity. *J. Geophys. Res. Ocean* **2012**, *117*, 4–13. [CrossRef]
48. Li, L.; He, Z.; Xia, Y.; Dou, X. Dynamics of sediment transport and stratification in Changjiang River Estuary, China. *Estuar. Coast. Shelf Sci.* **2018**, *213*, 1–17. [CrossRef]
49. Lee, S.-W.; Lee, D.; Noh, S.; Kim, G.-U.; Park, S.-H.; Jeong, J.-Y.; Lee, H.; Noh, J.H.; Jeong, J.; Lee, J.; et al. Sequential evolution of Changjiang Diluted Water and its impact on stratification and phytoplankton blooms in the East China Sea during summer 2020. *J. Geophys. Res. Ocean* **2025**, *130*, e2025JC022655. [CrossRef]
50. Geyer, W.R. The importance of suppression of turbulence by stratification on the estuarine turbidity maximum. *Estuaries* **1993**, *16*, 113–125. [CrossRef]
51. Wei, Y.; Wang, K.; Jin, H.; Yin, W.; Huang, D.; Xuan, J.; Wang, B.; Zhou, F.; Chen, J. Intermittent intrusions of Changjiang Diluted Water in Hangzhou Bay modulated by intraseasonal winds and tropical cyclones. *Estuar. Coast. Shelf Sci.* **2025**, *326*, 109525. [CrossRef]

Disclaimer/Publisher's Note: The statements, opinions and data contained in all publications are solely those of the individual author(s) and contributor(s) and not of MDPI and/or the editor(s). MDPI and/or the editor(s) disclaim responsibility for any injury to people or property resulting from any ideas, methods, instructions or products referred to in the content.